Final Report of the P̄ANDA PID TAG

Draft 0.7

G. Schepers, GSI Darmstadt, **et al.**

Contents

1   Introduction

The P̄ANDA ([1]) PID TAG (Particle Identification Technical Assessment Group) was installed to give to the collaboration a complete set of parameters for an optimal set of particle detectors. The task given to this TAG is described in more detail:

Subject

- − Requirements from physics
- − Evaluate potential of each subsystem
- − Matching of systems

Deliverables

- − Definition of global PID scheme
- − Optimized set of detectors and parameters

This list reflects roughly the structure of the PID TAG work and of this report. In an additional subsection the tools available for the PID TAG work are presented and explained (see also [2]) . The PID TAG evaluated the necessity of mapping the "Separation Power" in dependence of the momentum and the polar angle of the reaction products which is described in section 4.1. Since a "full simulation" was not available to calculate the performance of all the sub detectors, the TAG gathered parameterizations of the single sub detectors which went into a "Fast Simulation" explained in section 4.3. For single physics channels a "Full Simulation" was used.

Amongst others some important questions to solve were:

- • PID informations from the Central Tracker (Strawtube Tracker (STT) or Time Projection Chamber (TPC))

- • PID with and with out a Barrel ToF detector

- • PID with and with out an Forward Endcap Cherenkov, and with different forms (Focusing Disc DIRC, Time of Propagation Disc DIRC and Proximity RICH)

- • PID with and with out a Forward RICH

The PID TAG had about 10 presence meetings and over 20 online meetings. First PID subsystems were defined. Each subsystem has its responsible representative. Each representative had a replacement of his own group to guarantee always the same level of knowledge in all subsystems. For special subjects experts were asked to present informations in the meeting or to give answers to questions which arose.

The members of the TAG and their special responsibilities are listed at the end of the document (section 9).

2 Physics Requirements

The HESR (High Energy Storage Ring) of the new FAIR (Facility for Antiproton and Ion Research) project provides an Antiproton beam of high resolution (down to $\Delta p = 1 \times 10^{-5}$) and intensity from 1.5 GeV/c to 15 GeV/c momentum.

This offers the unique possibility of investigating a broad filed of physics. The vast variety of reaction types from meson-production over Charmonium decays to Hyper nuclear reactions demands a complete and compact detector system.

The physics requirements to the detectors are:

- to cover the full angular range of the physics products

- to detect all momenta of the reaction products

- to separate particle types with a defined level of separation over the full range of momenta of the reaction products.

The full solid angle can only be covered by the full set of detectors. Sometimes the momentum coverage has to be fulfilled by a combination of two or even three sub detectors.

For the single subsystems benchmark-channels had to be identified (Table 1) and simulated.

Channel	Final state	Related to detector
$\bar{p}p \rightarrow (n)\pi^+\pi^-$	$(n)\pi^+\pi^-$	EMC
$\bar{p}p \rightarrow \psi(3770) \rightarrow D^+D^-$	$2K\,4\pi$	DIRCs, ToF, STT/TPC
$\bar{p}p \rightarrow \eta_c \rightarrow \phi\phi$	4K	DIRCs, STT/TPC
$\bar{p}p \rightarrow D_S D_{S0}^*(2317)$	$\pi^\pm K^+K^-$	DIRCs, STT/TPC
		muon
		Forward RICH

Table 1: Benchmark channels to evaluate the performance of the different PID detectors.

At $\bar{\text{P}}$ANDA 2×10^7 reactions per second with up to 10 charged particles per reaction have to be digested by the detectors.

3   PID Subsystems

The different behavior of charged particles traversing active and passive detector material can be used to identify (on a probabilistic level) the nature of a charged particle. The PID detectors used in PANDA take advantage of the following effects:

- Specific Energy Loss. The mean energy loss of charged particles per unit length, usually referred to as dE/dx, is described by the Bethe-Bloch equation which depends on the velocity rather than momentum of the charged particle.

- Cherenkov Effect. Charged particles in a medium with refractive index n propagating with velocity $\beta > 1/n$ emit radiation at an angle $\Theta_C = arccos(1/n\beta)$. Thus, the mass of the detected particle can be determined by combining the velocity information determined from Θ_C with momentum information from the tracking detectors.

- Time-of-flight. Particles with the same momentum, but different masses travel with different velocities, thus reaching a time-of-flight counter at different times relative to a common start.

- Absorption. A thick layer of passive material absorb most particles due to electromagnetic (e+e-, γ) or hadronic interactions (all charged and neutral hadrons). After a certain amount of material only muons and neutrinos survive. The muons can then be detected easily with any kind of charged particle detector, depending on the desired speed and resolution.

The group of subsystems building the particle identification system of $\bar{\text{P}}$ANDA are listed with growing distance to the Target point:

- Time Projection Chamber

- Time of Flight

- Barrel DIRC

- Barrel Calorimeter

- Forward Cherenkov

- Forward Calorimeter

- Muon Counter

3.1 Central Tracker

Since the central tracker depending on the detector type provides as a surplus a dE/dx-information it can give important help for the particle identification in the low momentum regime (¡700MeV). For PANDA there are two options for the central tracker which is a Straw Tube Tracker on the one hand and a Time Projection Chamber on the other hand.

3.1.1   Time Projection Chamber (TPC)

The working principle of a GEM-based TPC and the geometrical design of the PANDA TPC [1] are sketched in Figs. 1 and 2. Charged particles traversing the detector volume ionize the counting gas and an electric field separates positive ions from electrons. The cylinder axis of the TPC coincides with the direction of the electrical field lines and also the direction of the solenoid magnetic field of the target spectrometer. The primary electrons are guided towards an amplification stage, which consists of a triple-GEM stack. No gating grid is foreseen for the PANDA TPC to allow a continuous operation at the HESR antiproton storage ring. In order to keep the build-up of space charge inside the drift volume at a minimum, the back flow of slow ions from the amplification stage has to be suppressed as much as possible. GEM foils [3] offer an intrinsic ion suppression if the settings of the whole stack are optimized accordingly. A continuous readout including online tracklet reconstruction is envisaged for the TPC.

In order to accommodate the target pipe, the TPC is split into two half-cylinders of a length of 150 cm. The inner and outer radius is 15 cm and 42 cm, respectively. 65 000 to 100 000 pads of an area of 4-6 mm^2 are planned. A Ne/CO$_2$ gas mixture (90/10), possibly with a small admixture of CH$_4$, and a gain of a few thousand are furthermore foreseen. The drift field is 400 V/cm. Under these conditions $\approx$ 50-100 energy loss measurements per track are feasible. This allows, in combination with a truncated mean algorithm, the identification of charged particles via their mean energy loss per track length dE/dx (Bethe-Bloch-formula, see equation 13). The TPC therefore contributes significantly to the overall PID performance of PANDA, in particular in the momentum regime below 1 GeV/c^2. In Fig. 3 the energy loss distributions for different particle types are shown up to 1.5 GeV/c^2. The plot has been obtained from the "Fast Simulation" described in section 4.3 assuming a dE/dx resolution of 8% for the TPC (cf. table 6).
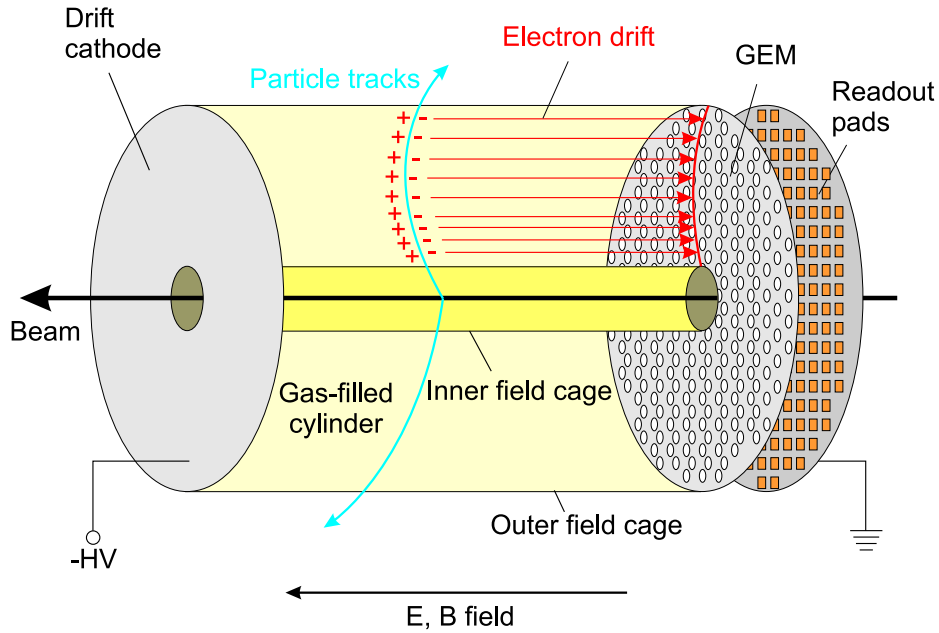

Figure 1: Working principle of a GEM-TPC (see text).
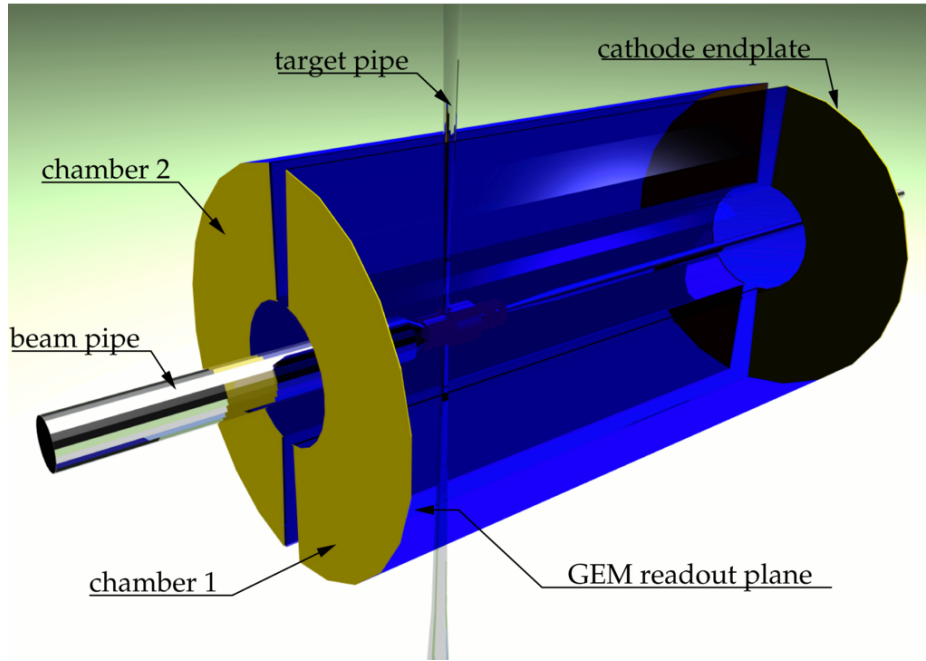
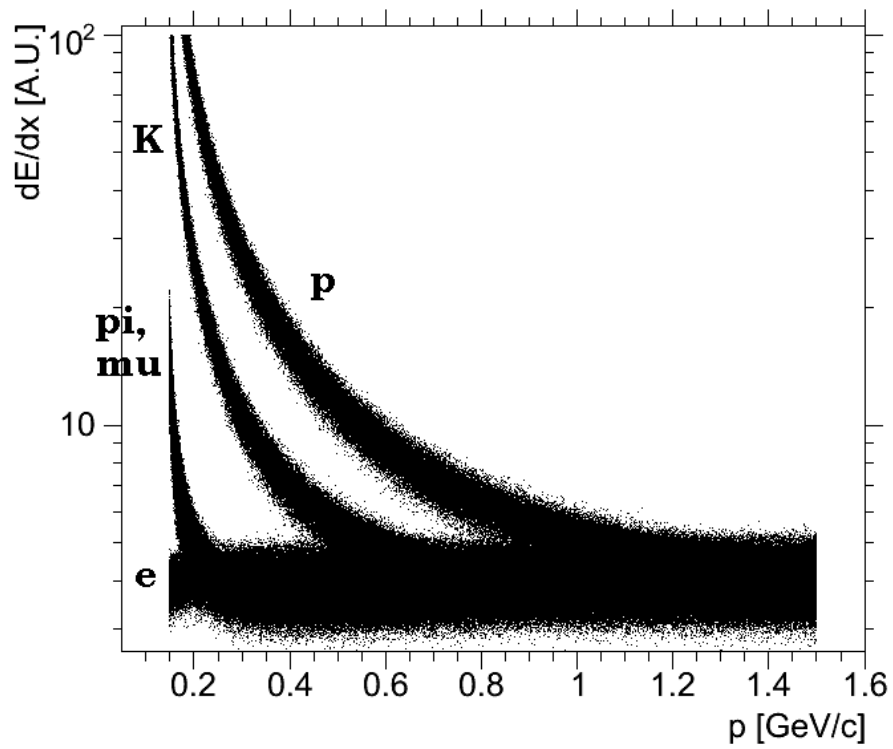Figure 2: Geometry of the PANDA TPC; for further details see text and [1].

Figure 3: Energy loss in the TPC vs. particle momentum up to $1.5\,\mathrm{GeV}/c^2$.

₁₄₅ ### 3.1.2   Straw Tube Tracker (STT)

3.2 Time of Flight (ToF)

Barrel Time-Of-Flight

Barrel Time-of-Light detector (TOF) has to be placed inside solenoidal magnet and provide identification for soft particles at large polar angles from 22 to 140 degrees. The recently developed timing Resistive Plate Chambers (RPC) represent currently the optimal choice for Barrel TOF detector that in principle offers the required resolution of better than 70 ps. The identification of pions, kaons and protons is possible up to few GeV/c.

A stable operation of the such RPCs was observed in extensive tests during many years in various experiments. The RPCs were found to be fully efficient and low-noise chambers. One of useful feature of the RPC is its immunity to magnetic field. Proposed here design is based on experience obtained during work for the HARP experiment[1]
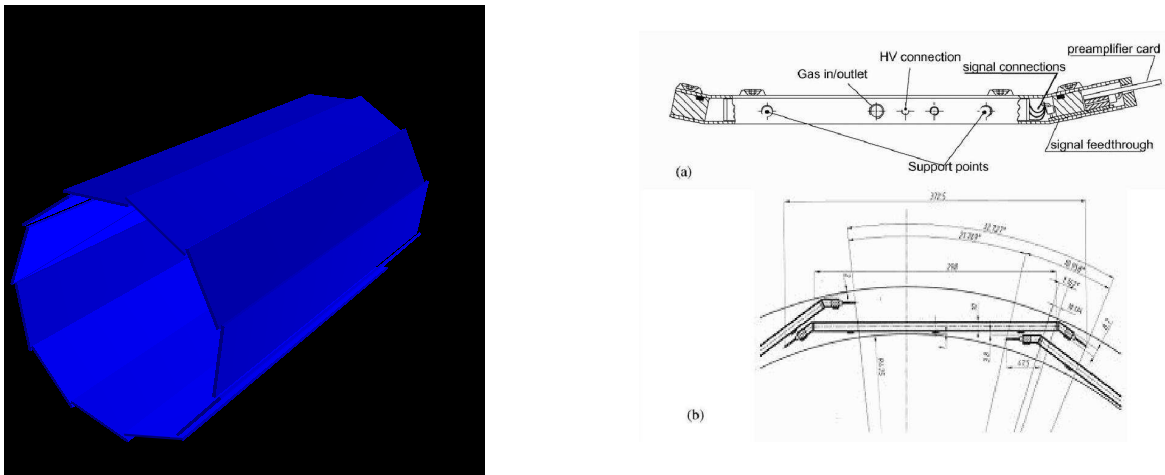

Figure 4: 3D-view and (right)- possible arrangement of 11 barrel RPCs.

Geometry. The RPC-TOF consists of 11 modules arranged around TPC (or STT) in the way shown schematically in fig.4(left) Length of each module is $\sim 190\ cm$, width of its active area is $\sim 30\ cm$. Each module is multi-gap glass RPC placed inside aluminium case. To have full coverage in azimuthal angle, active areas of neighbour modules will be overlapped as it shown in fig.4(right). PCB with FEE electronics will go along both long sides.Total sensistive region of the Barrel RPC-TOF is about $7\ m^2$.

Four-gap RPC design. Because of hard demands on amount of material for the Barrel-TOF detector, four-gap glass RPC was chosen. Cross-section of 4-gap RPC is shown schematically in fig.5 taken from [1]. The RPCs can be made from a "standard" float glass with thickness of $0.6\ mm$ and with bulk resistivity of $\sim 10^{13}\Omega cm$. The gaps between glass plates are kept with spacers made of fishing line. RPC contains two identical sets of three glass plates and two $0.3\ mm$ gas gaps. High voltage is applied to the outer glass plates through graphite coating. The read-out strips are made with 15 μm Cu on 75 μm Kapton. All "reference" strips placed on both outer plates of glass stack have to be connected to ground. Glass RPC are housed in an aluminium case made with 1 mm thick aluminium plate. Full thickness of a module is 10 mm only. O-ring

provides gas tightness. Beam test[2] of four-gap RPCs has demonstrated that time resolution of $\sim 75\ ps$ can be reached even with old HARP FEE.

Readout electrodes and FEE. Each RPC will equipped with 64 strips with double ended readout. Each strip have a length of $\sim 30\ cm$ at $30\ mm$ width. Already existed data[3] on multi-gap RPC with strips (strip length: 95 cm and width: 25mm) inspire a hope that time resolution of 60-70 ps can be reached with double-end readout. Signals will be amplified and digitized at the RPCs to use the Time-Over-Threshold (TOT) method for slewing correction as it was proposed in[4]. Number of TDC channels needed to read each RPC is 128, all strips is 1408. The development of the read-out system has to be a major task during $R\&D$ study for the PANDA RPC.
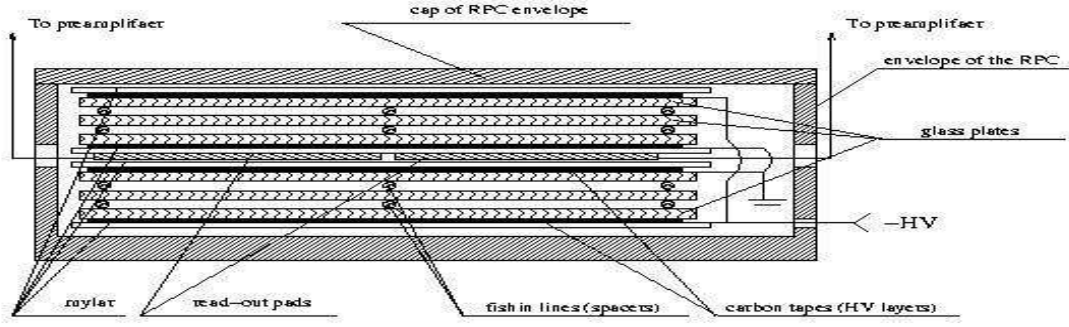

Figure 5: Four-gap RPC. Cross-section through its short side.

Gas system. Set of eleventh TOF modules having total gas volume of ~ 60 liters is operating with a non-flammable gas mixture containing $90\%R134A$, 5% isobutane and $5\%SF_6$. The flows of three gas components are metered with "electronic mass flow meters". At total flow rate of about $200\ cm^3/min$, a gas exchange of one volume will be every ~ 5 hours. The TOF modules are supplied with gas in groups, say, of four. Each group has its own control and protection systems.

Material budget. Radiation length for a module containing 4-gap glass RPC is given in Table 2. It was assumed that RPC is made of 0.6 mm thick glass. Radiation length X/X_0, calculated in the Table is only given for a particle which crosses a TOF module perpendicular to its plane.

Table 2: Thickness of the TOF detector.

material	$X_0(mm)$	thickness(mm)	X/X_0
glass	127	3.6	2.83%
aluminium	89	2	2.22%
copper	14.4	0.1	0.69%
mylar	287	0.6	0.21%
kapton	286	0.25	$\sim$0.10%
		Sum	$\approx 6.0\%$

Rate capability. Very important question is the rate capability. Since the bulk resistivity of glass is $\sim 10^{13}\Omega \cdot cm$, the rate capability of a glass RPC could bring a potential problem due to

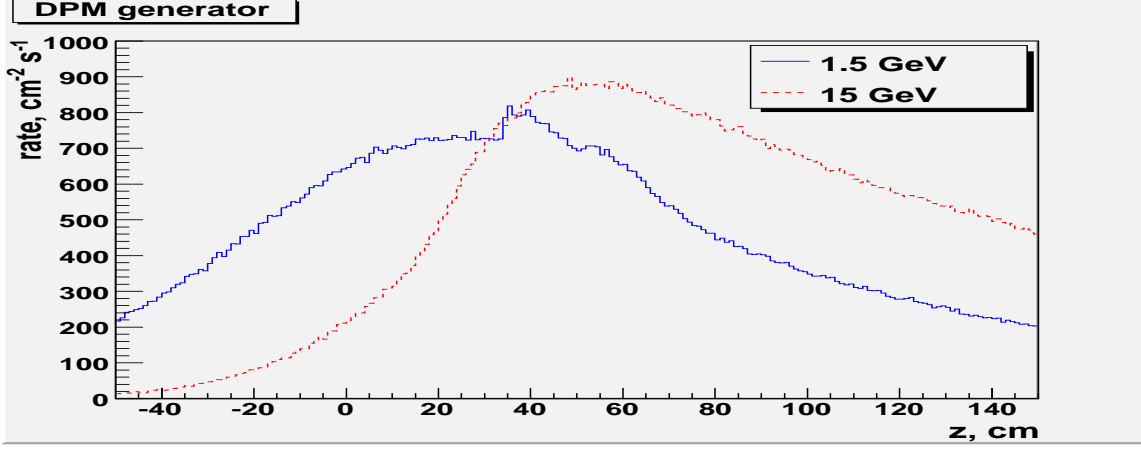192 the time needed to neutralize the charge deposited on the resistive plates after discharge inside
193 gas gaps.

Figure 6: Expected values of partcle fluxes calculated for two values of insident particle momentum:
1.5 GeV/c and 15 GeV/c .

194 During $R\&D$ work for the HARP experiment, one small four-gap RPC was tested against particle
195 rate in the T10 beam area at CERN. It was found that the RPC works well at 500 Hz/cm^2.
196 More precise measurements have been done in the GIF test area for the ALICE TOF detector. It
197 was observed that there was no deterioration of the efficiency and the resolution for the ALICE
198 MRPCs up to 1 kHz/cm^2. This result found for 10-gap glass RPC should be well for 4-gap
199 chamber too. Expected particle flux in the PANDA barrel is shown in fig.6 for two values of the
200 incident anti-proton momentum: 1.5 GeV/c and 15 GeV/c. In both cases a maximal particle rate
201 is less than 1 kHz/cm^2. The estimation was done using Dual Parton Model generator for minimal
202 bias events.

Particle Identification. The Barrel RPC-TOF provides a particle identification using a mea-
surement of a particle arrival time and a momentum and length of a track information from the
tracking detectors (TPC or STT). A mass of a particle, m, can be determined from the particle
momentum, P, the particle track-length, L and a measured time-of-flight, t, as

$$m \;=\; \frac{P}{c} \cdot \sqrt{\frac{c^2 t^2}{L^2} - 1},$$

203 where L and P are measured with a tracking system. A possibility to discriminate between a
204 lighter and a heavier particle of same momentum depends on time resolution, σ_t, of the TOF
205 detector.

At simulations of the RPC-TOF performed in PandaRoot framework, signals are produced when
a track of a charged particle penetrates the RPC. One signal is going to the one end, the other
signal - to the other end of a strip. A velosity of the propagation is equal 19.05 cm/ns. Times $t1$
and $t2$ when the signals will reach the ends are given as

$$t1 = t + (l/2 - x)/v, \qquad t2 = t + (l/2 + x)/v,$$

206 where l is the width of the cell (29.8 cm), x is the x-coordinate of the track in the local system
207 of the strip. The time t when the particle crosses RPC can be taken as $(t1 + t2)/2$. If each of the
208 times $(t1,t2)$ is distorted with dispersion 100 ps, then the time resolution σ_t is equal $\approx$ 70 ps.

In the PandaRoot framework, we generated events of K, Pi, proton production isotropically through the RPC-TOF with momenta from 0.1 to 2.1 GeV/c. We simulated and reconstructed the events using RPC-TOF, and calculated velocity and squared mass of the particles by formulas: $1/v = t/l$ and $M^2 = P^2(1/v^2 - 1)$. Figs. 7, 8 give results of a particle identification using $1/v$ and M^2 information from the RPC-TOF.
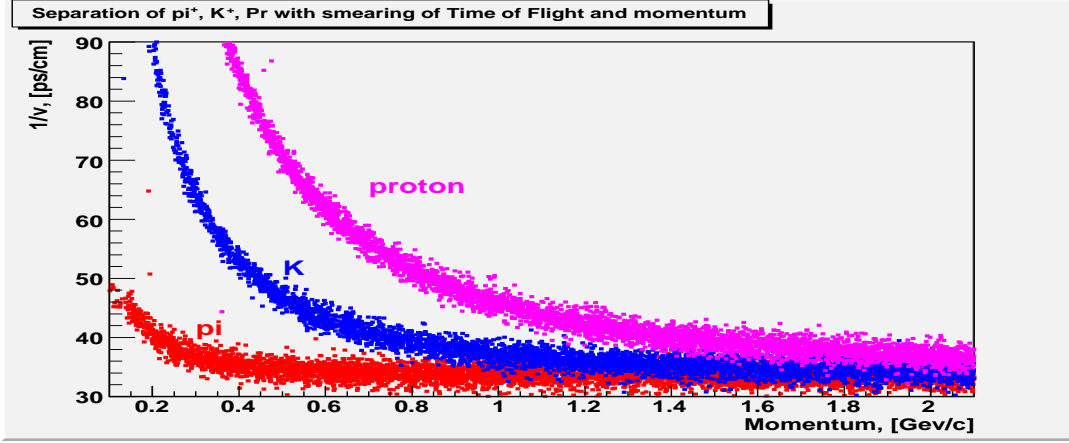

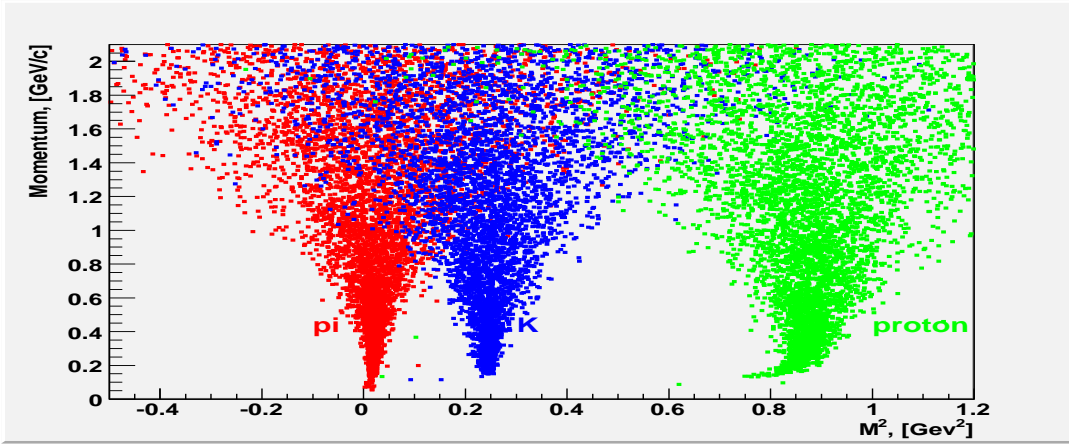Figure 7: Inverse velocity of particles reconstructed with RPC-TOF vs. momentum.

Figure 8: Momentum of particles vs. squared mass reconstructed with RPC-TOF.

Separation power. Fig.9 shows calculation of a separation power. Difference between time of flight of two different particles divided by the TOF resolution, $(t_1 - t_2)/\sigma_t$ ("separation power"), is presented in this figure for different pairs of particles for the most hard case - for polar angle $\Theta = 90^0$, and for polar angle $\Theta = 30^0$. The computation was done for two values of σ_t: 70 ps and 100 ps.

The calculations of the separation power for angle $\Theta = 30^0$ demonstrate that the barrel TOF with resolution of $\sim 70 \ ps$ will be able identify hadrons with momentum up to few GeV/c. The RPC-TOF providing the particle identification at low momentum, especially at angle Θ close to 90^0 is supplementary to the TPC/STT and DIRC detectors.

Now it is important to understand how the RPC -TOF separation capability is matched with hadron momentum spectra in the Barrel region. Fig.10 shows proton, K- and π-meson momenta
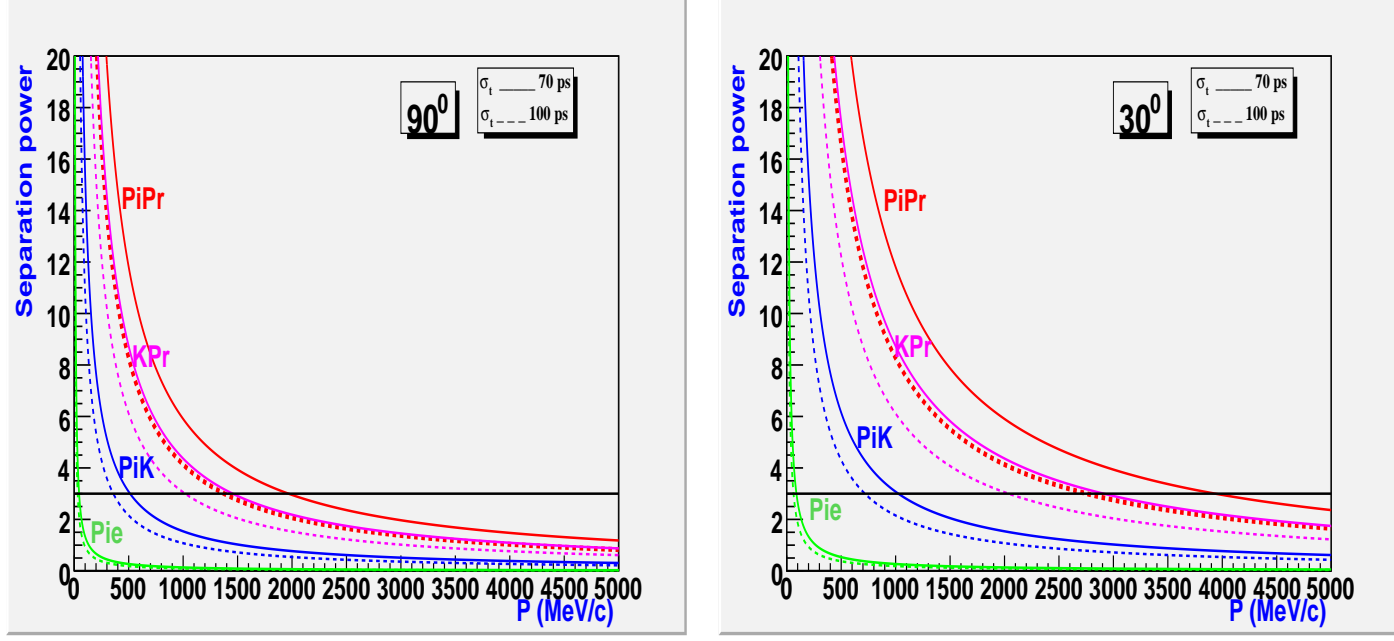
Figure 9: Separation as a function of momentum for polar angles $\Theta = 90^0$ and $\Theta = 30^0$.

simulated by DPM in minimal bias versus the Barrel polar angle plots for $\bar{p} - p$ events at 15 GeV/c by DPM in minimal bias as most hard case. For the proton plot, the solid line is the 3σ proton/kaon separation curve. For the pion plot, the 3σ kaon/pion separation curve is shown. For the kaon plot, it is needed to show 2 curves - for the 3σ proton/kaon separation (solid line) and the 3σ kaon/pion separation (dotted line). Separation curves are calculated for the 70 ps time resolution. It is clearly seen that the Barrel RPC-TOF is very suited for the charged hadron identification in most populated momentum regions and leaves some room for the identification by the DIRC in rare populated regions of high momenta at small polar angles. Thus, the RPC-TOF and the DIRC supplement each other for small polar angles in the Barrel. Furthermore, the RPC-TOF can help as a reference detector for the one-dimentional DIRC identification for high particle momenta at small barrel polar angles.

In ideal case, the time-of-flight is measured with information from two detectors: start time, t_0, from a reference detector placed somewhere near target and stop time t from the barrel TOF. However, even in case of no start detector, t_0 can be found by fitting measured values of t in multiparticle events with different hypothesis.

References

[1] "The HARP resistive plate chambers: Characteristics and physics performance", V.Ammosov et al., NIM **A578** (2007) 119-138

[2] "Four glass RPC as a candidate to a large area thin time-of-flight detector", V.Ammosov et al., preprint IHEP 2002-10, Protvino 2002

[3] "Prototype Performance on Novel Muon Telescope Detector at STAR", Lijuan Ruan (for the STAR), 24th Winter Workshop on Nuclear Dynamics, South Padre, USA, April 5-12 2008

247 [4] IHEP+JINR proposal, PANDA Workshop, ITEP, Moscow, April 17-18 2008,
248    $http://www-panda.gsi.de/html/panda\_russia/HARP\_PANDA\_ITEP.ppt$
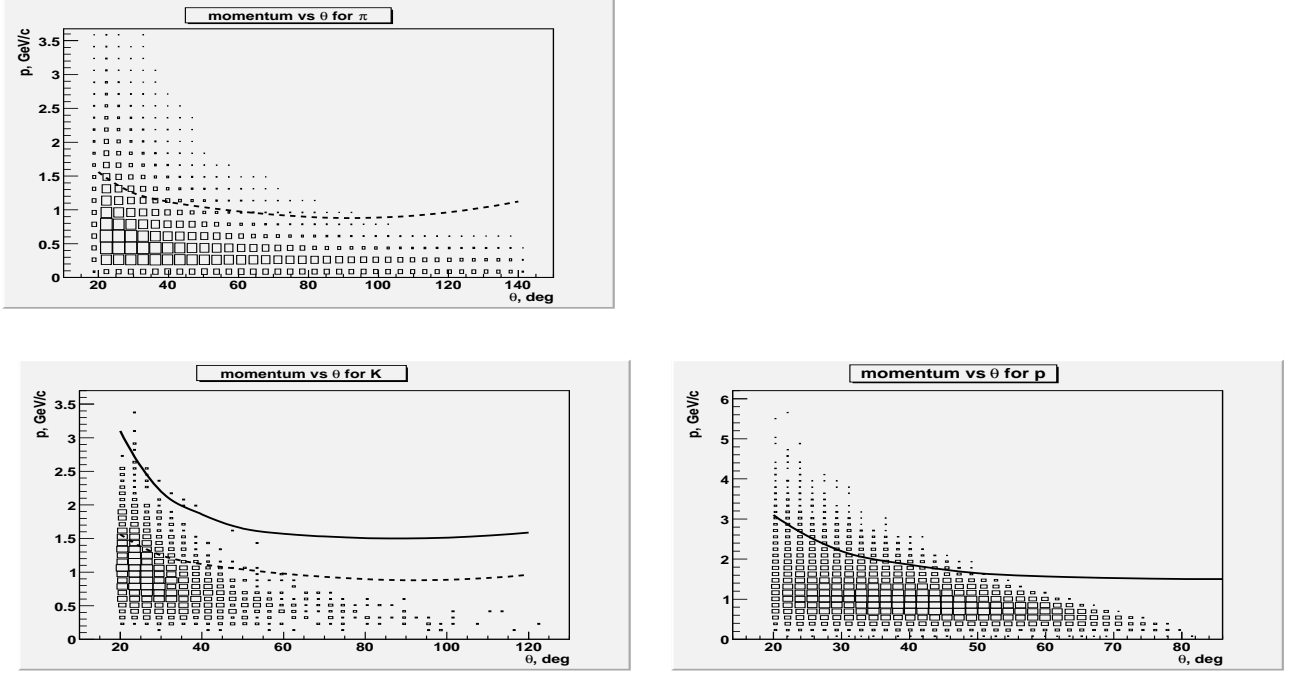

Figure 10: P vs θ particle population plots and 3σ separation curves for the 15 GeV/c DPM events.

3.3 Barrel DIRC

The purpose of the Barrel DIRC (Detection of Internal Reflected Cherenkov photons) is to provide a particle identification. The mass of the particle can be achieved by combining the velocity information of the DIRC with momentum information from the tracking detectors. In addition the distinction between gammas and relativistic charged particles entering the EMC behind the DIRC is possible.

Basis for the calculations and simulations are the bar dimensions taken from the BaBar DIRC [4]. With the length adapted to the $\bar{\mathrm{P}}$ANDA setup there are quartz bars of $17 \times 35 \times 2300\ mm^3$ and a distance of 480 mm to the target point. Thus the barrel DIRC covers the solid angle between 22 and 140 degrees. The lower momentum threshold for kaons which produce Cherenkov light is for an envisaged refractive index of n=1.47 as low as 460 MeV/c for single photon production. For larger photon numbers the threshold increases.

With 17mm (of thickness) of fused silica the DIRC bars present approximately 14% of a radiation length to normal incident particles. The support structure will add 3%.

This design is initially based on the BaBar DIRC [4] but at $\bar{\mathrm{P}}$ANDA further improvements of the performance are under development. The combination of the spatial image of the photons with their time of arrival gives access not only to their velocity but also to the wavelength of the photons. Thus dispersion correction at the lower and upper detection threshold becomes possible. Further on the reduction of the photon readout in size and number of photon detectors is envisaged. A lens or a set of lenses at the exit of the quartz bar focus the photons to a focal plane behind a readout volume of about 30 cm length. When this volume is filled with a medium with the same refractive index as the radiator material (n_{medium}=$n_{radiator}$=1.5) additional dispersion effects and other image distortions are avoided.

A major issue is the maintenance of the barrel DIRC. While in the Babar DIRC a removal of the radiator barrel and the photon detector was not foreseen, the PANDA barrel DIRC is planned removable. The removal is not planned as default operation during maintenance breaks. Rather the access to other detector parts and the replacement of broken DIRC items need a removal procedure. For that purpose a photon detector smaller in size is favorable. The segmentation of the radiator barrel and the optical joints between radiator and photon detector need also careful design. As shown below the design of the photon detector and its link to the radiator define the geometric dimensions of the latter.

280 3.4 Barrel Calorimeter

3.5   Forward Cherenkov

Two DIRC design options exist for the endcap part of the target spectrometer section. These differ in the photon readout design but both use an amorphous fused silica radiator disc. The endcap detector position covers forward angles of up to $\vartheta = 22°$ excluding an inner rectangular **(is it now elliptical??)** area of $\vartheta_x = 10°$ horizontal and $\vartheta_y = 5°$ vertical half-angles. Simulations using the DPM generator [5] give 1.0±0.8 (at 2 GeV/c) to 2.3±1.8 (at 15 GeV/c) charged particle multiplicity per $\bar{p}p$ interaction emitted from the target vertex into this acceptance.

In such a one-dimensional[1] DIRC type, a photon is transported to the edge of a circular disc while preserving the angle information. Avoiding too much light scattering loss at the surface reflections requires locally (in the order of millimeters) a surface roughness not exceeding several nanometers RMS.

The lower velocity threshold, which is common to both designs, depends on the onset of total internal reflection for a part of the photons emitted in the Cherenkov cone.

There are several boundary conditions for the disc thickness. Radiation length considerations as the detector is upstream of the endcap EMC call for a thin disc. The focussing design is workable with a 10mm thickness (X_0=126mm). Regarding the mechanical stability and handling during polishing, current company feedback recommends 20mm minimum thickness. The resulting thickness of the radiator disc has to be a compromise.

---

[1]Light is only reflected on surfaces of one spatial orientation, here the two disc surfaces both normal to the z axis.

3.5.1 Focussing Disc DIRC

In the Focussing Light guide Dispersion-Correcting design (Figures 11 and 12), when a photon arrives at the edge of the circular or polygonal disc, it enters into one of about hundred optical elements on the rim. Here the two-fold angular ambiguity (up-down) is lifted, the chromatic dispersion corrected and the photon focused onto a readout plane. While the optical element entered determines the ϕ coordinate, measuring the position in the dispersive direction on the focal plane of the focussing light guide yields the θ coordinate.
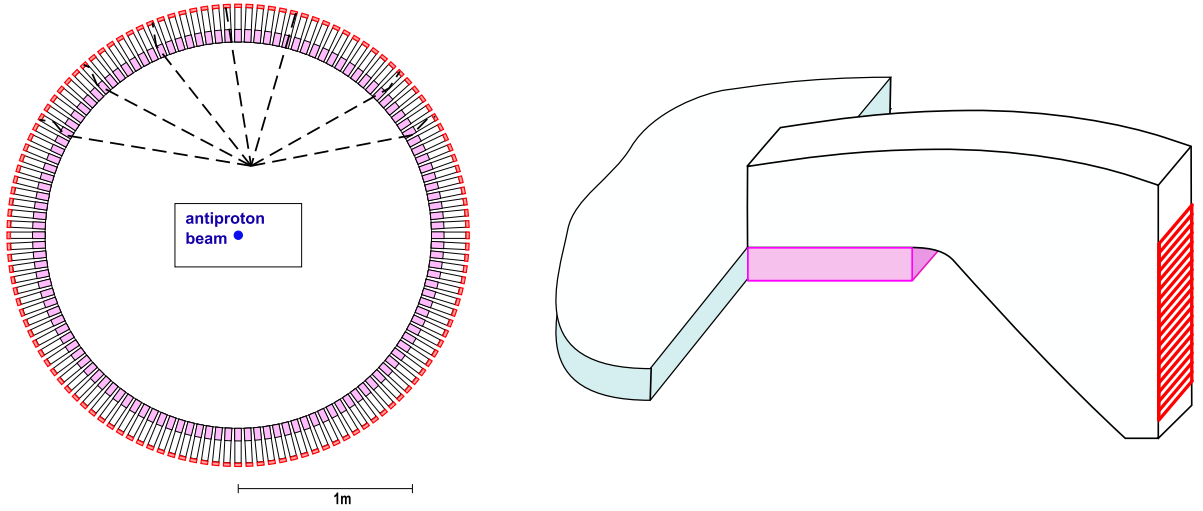
Figure 11: Polygonal disc with focussing light guides attached to the rim used as optical readout components.

Lithium fluoride (LiF) is UV transparent and has particularly low dispersion. Proton beam irradiation of a test sample shows that radiation-produced color centers are confined to sufficiently small wavelength ranges, and are only partially absorbing at the expected $\bar{P}$ANDA lifetime dose. Hence we believe we can use LiF as a prism element (see Fig. 12) to correct the Cherenkov

Figure 12: Light guide side view shown with a set of rays used for optimising the light guide curvature. Reflections at the parallel front and back surfaces keep the light inside but do not affect the focussing properties.

Figure 13: Simulated photon hit pattern for four particles emitted at different angles θ and ϕ from the target vertex.

Figure 14: Simulation-derived pion-kaon separation power for a focussing lightguide design with a 15 mm thick amorphous fused silica disc and 0.4 eV photon detection efficiency. Calculation February 2008.
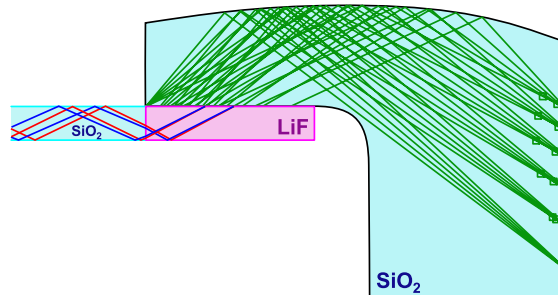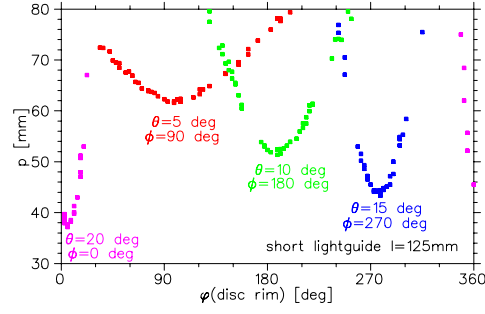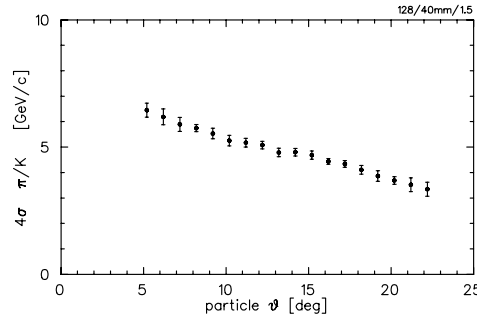
radiation dispersion. The two boundary surfaces, with the radiator disc and the subsequent light guide, make the chromatic dispersion correction angle-independent to first order.

As with the radiator, the light impinging on the inside of the light guide's curved surface undergoes total internal reflection, hence no mirror coating is needed. This reflection makes the focussing also independent of the wavelength.

With the light staying within the dense optical material of the light guide, most of the incoming light phase space from the disc is mapped onto the focal plane with its one-coordinate readout. The focussing surface with cylindrical shape of varying curvature has been optimised to give an overall minimum for the focus spot sizes of the different angles on the focal plane, individual standard deviations being well below 1 mm for the instrumented area.

For an Endcap DIRC detector with 128 lightguides and 4096 detector pixels that fits inside the target spectrometer return yoke, Figure 14 shows the angle-dependent upper momentum limit being about 4–6 GeV/c for 4σ pion-kaon separation within the acceptance ϑ=5°–22°.

Typically all of the 40 detected photons per particle arrive within a 4 ns time window.

Each lightguide can individually be assigned its own 0.4 ns acceptance window. For the pixel size used in this simulation they are contained inside a 40 pixel·ns volume, which at 4K detector pixels amounts to 10 ps detector occupancy time per particle signature.
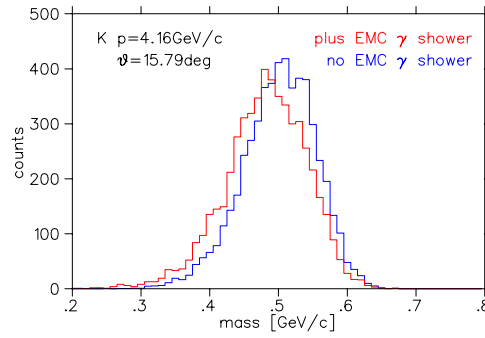
Figure 15: Left: Measured photon distribution from a γ Barrel EMC shower leaking out of the EMC edge towards the Endcap. Photons from one kaon of 4.16GeV/c^2 are added, and the kaon velocity is derived from candidate kaon photons. Right: Analysed mass distributions for kaon with and without shower. The road for kaon photon acceptance is derived from simulations, and within some simulation simplifications the bounds are set such to include (almost) 100 percent of the photons. The systematic offset with the onset of background is though to be caused by the true kaon photon centre of gravity being off the middle of the road interval, probably explained by the coma aberration of the curved lightguide focussing (an improved interval algorithm should help). At this level of background there is a small increase in the width of the reconstructed kaon mass distribution.

The detected photon rate (source: presentation KF 2007-03-27 Genova, 2E7 interactions; scaled to 4K pixels) is 3E7 s^{-1} per PMT and 1E6 s^{-1} per detector pixel.

Figure 16: Sketch of the flight-path in the ToP Disc

3.5.2   Time of Propagation Disc DIRC

In the Multi-Chromatic Time-of-Propagation design ([6]) small detectors measure the arrival time of photons on the disc rim, requiring σ_t=30–50 ps single photon time resolution. For any given wavelength, the disc edge is effectively covered alternately with mirrors and detectors. Only due to the resulting different light path-lengths one can determine accurately enough the start reference time, i.e. the time when the initial charged par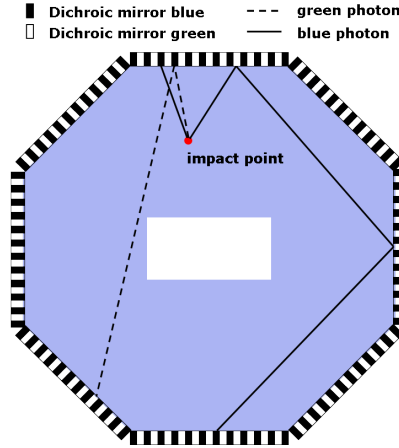ticle enters the radiator, as the stored anti proton beam in the HESR has no suitable time structure to be used as an external time start.

As some of the light is reflected several times before hitting a detector, the longer path lengths allow a better relative time resolution.

The use of dichroic mirrors as color filters allows the use of multiple wavelength bands within the same radiator (the current design suggesting two bands) resulting in higher photon statistics. The narrow wavelength bands minimize the dispersion effects, and the quantum efficiency curve of the photo cathode material could be optimized for each wavelength band individually.

To verify the Principe of TOP DISC the geometry of the disk was implemented into PANDAROOT system and multiple set of Monte-Carlo data was generated with subsequent reconstruction of generated particle type. The fig.17, below shows the DISC implementation into PANDAROOT(left) and generated photons from incident pion and their path from impact point on disc(right).

Reconstruction of particle types using different methods, like Pattern fitting or Slope fitting in two-dimensional(detector number and time of propagation(fig.18) in first case, the calculated arrival time of Cherenkov photons and MC time from GEANT in second case) space yields acceptable separation and low percentage of misidentification. See fig.19 for example in case of Kaons and Pions.

Already first simulations indicate the possible hurdles in particle identifications in DIRC. One of them is the smearing of the patterns from secondary particles, marked as blue points in fig.18. The possible effect from this is depicted on next figures, where we present the misidentification between Kaons and Pions without inclusion of secondaries, see fig.20 and with inclusion of them ,see fig.21.
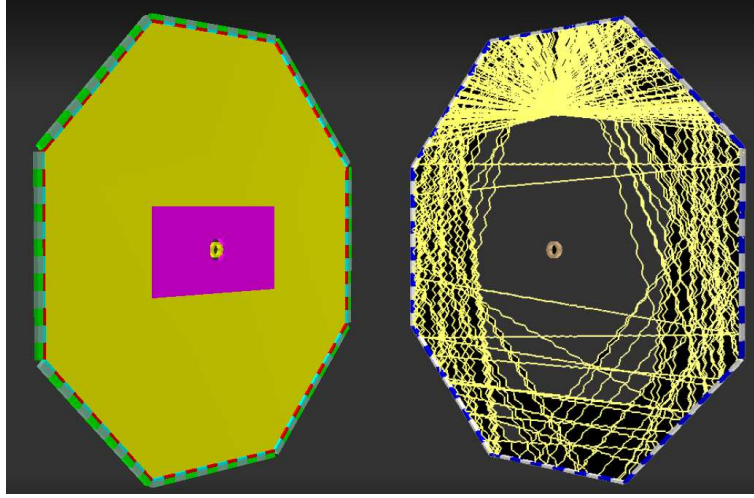
Figure 17: Current scheme of TOP DIRC, 960 photon detectors mounted at rims of octagon disc, located at 180cm from Z=0 point in PANDA coordinate system(left side). On right side disc was hit by 4 GeV/c pion at 15°, the yellow lines shows the path of generated Cherenkov photons. Some of them, if they hit dichroic mirrors, gets reflected and travel longer.

To check the effect of this one and to measure the time resolution of possible candidates for photon detection , $MCP - PMT's$ from Budker Institute of Novosibirsk in real beam situation, we have scheduled TestBeam measurements on DESY site with electron beams in energy range between 1-6 GeV/c. To show that electrons can imitate Cherenkov radiation like Pions we have performed MC simulation of passage of pions and electrons through 2cm thick quartz glass. The resulting spectra are depicted in next fig.22. As we can see $\approx 60\%$ of electrons pass the glass without showering(red spectra), like most of the pions(magenta spectra). In both cases we have secondaries , significantly more from electrons(blue) than from Pions(green). This is the more difficult situation than in case of pions, but for the test, its better to have checks done in difficult case than in simplified ones. The time resolution, that we want achieve in PANDA final design, is a subject for the Lab tests before Test beam. As it will have not only the component coming
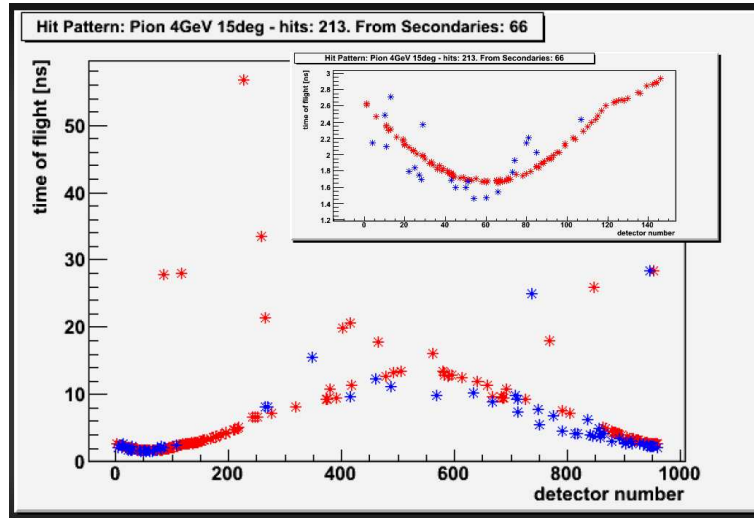
Figure 18: Hit pattern of photons in two-dimensional(ϕ,t) space. The Cherenkov photons coming from primary particle are marked red and from secondary particles , marked blue.

from MCP-PMT's, but also from neccesary electronics, their contribution was tested in the Lab using approximately the same chain as it awaited in final electronic design, see fig. 23. Currently, with available electronics, we achieve $\approx$ 40 ps resolution as it depicted in next fig.24, along with electronic scheme(fig.23) used in measurements.
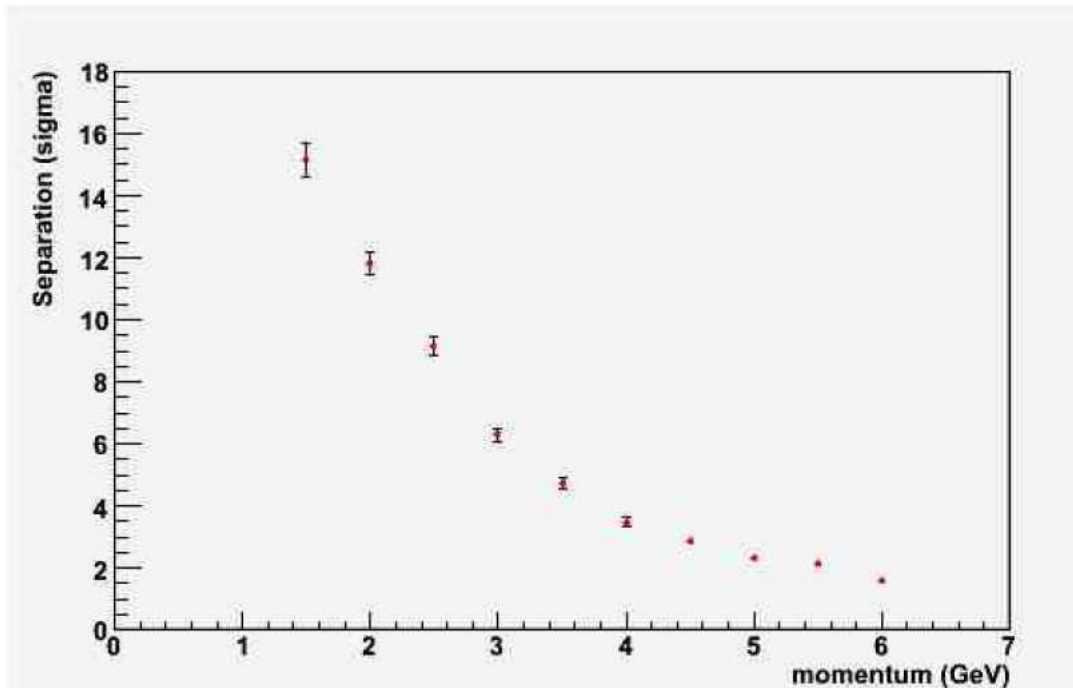
Figure 19: Separation power between Kaons and Pions from Slope fitting.
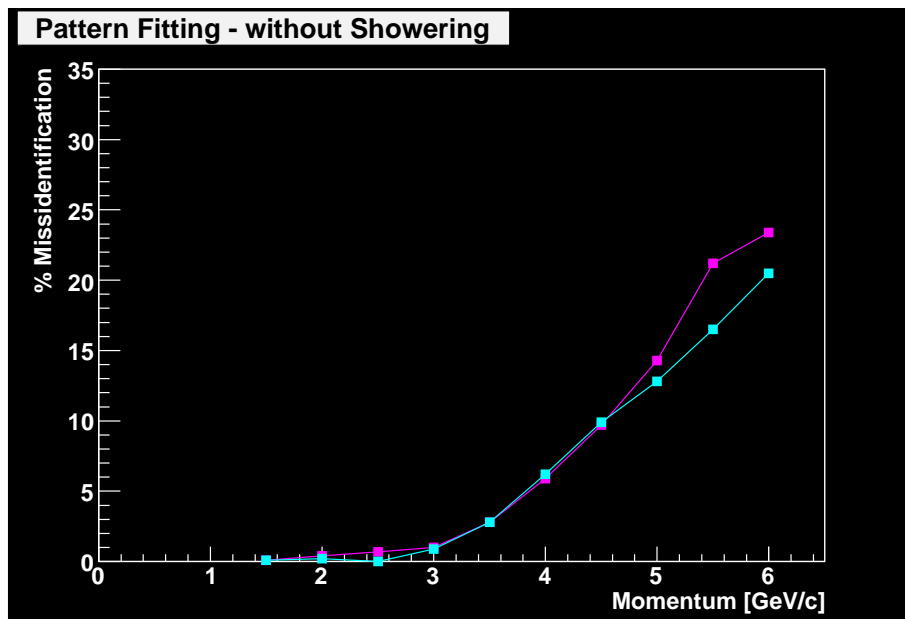
Figure 20: Misidentification between Kaons and Pions without inclusion of Cherenkov photons from secondaries into reconstruction.
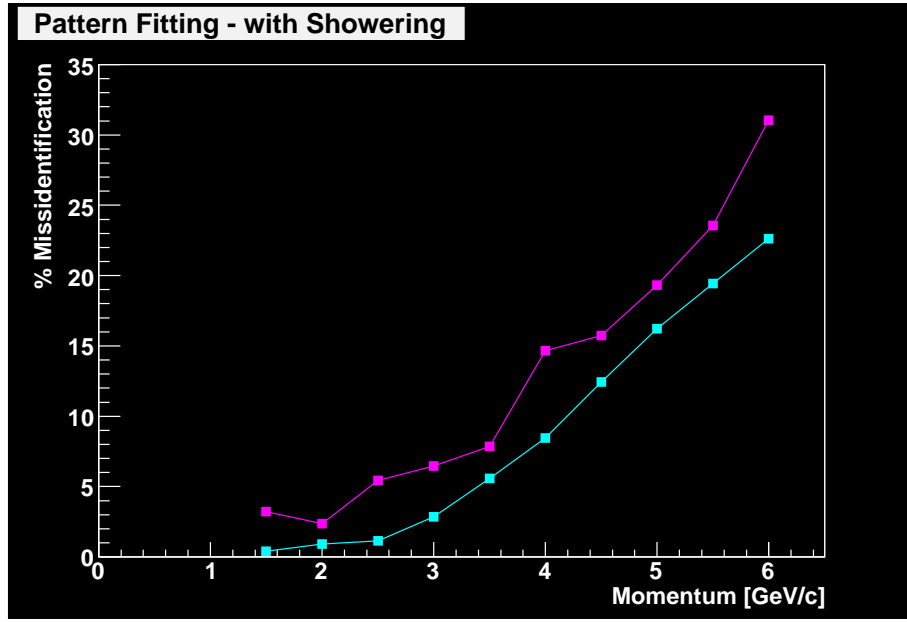
Figure 21: Misidentification between Kaons and Pions with inclusion of Cherenkov photons from secondaries into reconstruction.
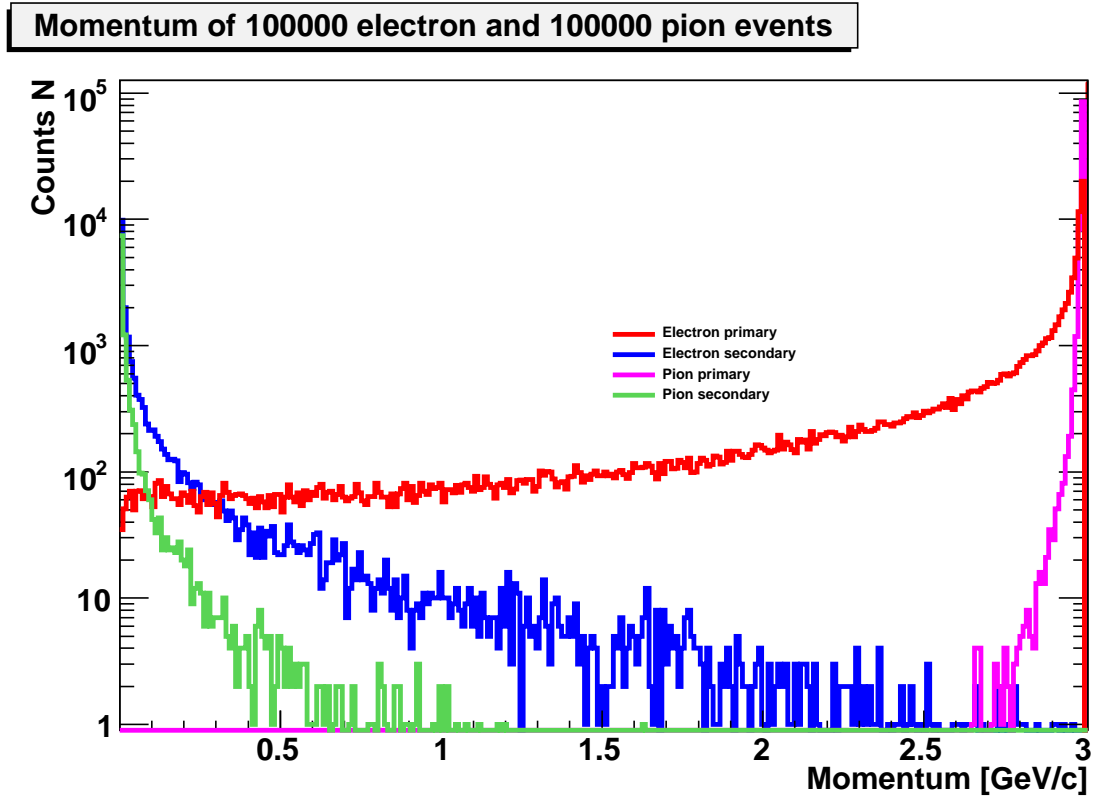
Figure 22: Energy spectra of primary and secondary charged particles inside 2cm thick glass after hitting it with electrons(pions) with 3.0 GeV energy. Unfortunately the energy of secondary particles are high enough to create Cherenkov photons and as they doesn't have the same direction as the primary particle, the photons created by them smear coordinate or timing pattern of primary particle, hence, making reconstruction difficult.
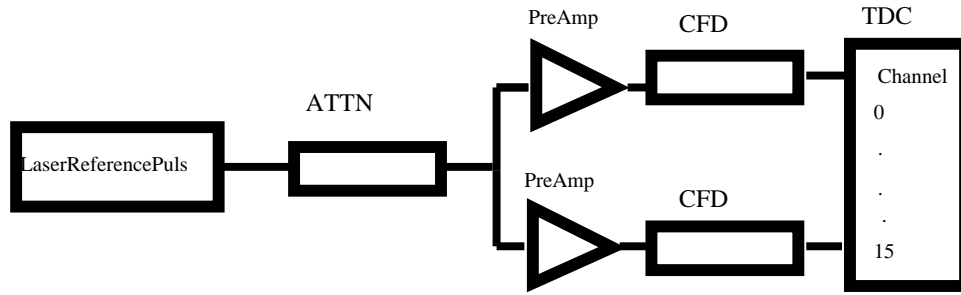
Figure 23: Used electronic scheme to measure contribution of each electronic module in time resolution. Note that TDC 1 channel is 25 ps.
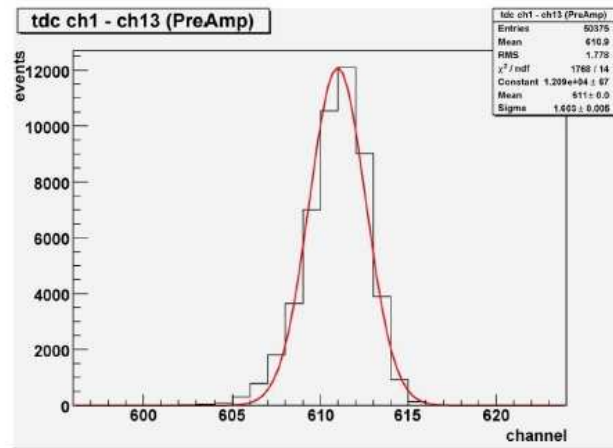
Figure 24: Achieved time resolution in TDC channels. Note that TDC 1 channel is 25 ps, and a Gaussian fit yields a Sigma of 1.4 channel.

3.5.3 Proximity RICH

As alternative approaches Proximity Imaging Solutions were considered.

- Liquid radiator proximity RICH using CsI GEMs: Proximity focusing RICH detectors use the most simplest imaging geometry. Their resolution depends on the optical quality and crucially on the ratio of radiator thickness to stand-off distance, the distance between the creation and detection of the photon. Using liquid or solid radiators yielding enough Cherenkov photons, the radiator can be kept rather slim, which in turn only require moderate stand-off distances on the order of 100 mm. The ALICE HMPID detector is build in this fashion using a C6F14 liquid radiator and CsI-photon cathodes in an MWPC. This requires a UV optic. It is proposed to use the same radiator technique and combine the third tracking station with a CsI coated GEM photon detector. The detector will be thicker along the beam direction than the DIRC detector previously described, but can be essentially moved to any position along the beam axis. The estimated performance and the ALICE/STAR test results show a significant decrease in performance compared to the DIRC solutions.

- Solid radiator proximity RICH using CsI GEMs: One of the main drawbacks of using the ALICE design is the use of C6F14. This radiator is rather sensitive to impurities and radiation damage requiring a purification system. Using a fused silica disc with a properly machined surface as radiator circumvents the problem while keeping the geometrical advantages of the design. Initial studies show a further reduction of performance mainly due to strong dispersive effects in the UV region.

- Aerogel proximity RICH using PMTs: The Belle endcap Cherenkov threshold counter will be replaced by a proximity imaging RICH counter using an Aerogel radiator and conventional BiAlkali based multi-pixel PMTs as photon detectors. Using a so-called focusing radiator scheme, prototypes show excellent performances. The main technological challenge for this detector is to realise a photon detection matrix in a strong magnetic field. Recent developments in the field of proximity focusing HAPDs seem to make such a detector realistic. The large number of pixels required should the detector be placed behind the EMC, but inside the cryostat merit a detailed look at the costs of such a design.

400 **3.5.4 Forward RICH**

3.6   Forward Calorimeter

3.7 Muon Counter

The main purpose of the PANDA muon system is to achieve the highest efficiency in identification of muons in the medium-high energy range. Muons are present in the final state of many annihilation channels. Among them the physics program is mostly concentrated on dimuon production from Drell Yan at the maximum HESR momentum of 14.5 GeV/c or J/ψ formation and decay in nuclear matter at 4.1 GeV/c momentum. In addition the study of rare decay of charmed particles could require a single muon identification. The most severe PID requirements to the muon system are set by the DY dimuon production, that has been selected as benchmark channel. Looser identification requirements are set by the J/ψ production channels, because of the strong kinematics constraint on the dimuon mass.

In general the interesting processes having muons in the final state have small cross section compared with the background, e.g. the DY channel features a very low cross section ($\approx 1nb$) and the unfavourable signal-to-noise ratio ($\approx 10^{-6}$). As a consequence the muon system must provide the maximum acceptance and efficiency. In the dimuon channels the simultaneous identification of a slow and of a fast muon is needed, with a strong correlation angle-momentum.

Muon counters are foreseen both in the Target barrel part and endcap. In the Forward spectrometer the muon counters and filters will act as hadronic calorimeter. The azimuthal angle covered by the muon system ranges from 0° to 120° with a 2π polar angle coverage. With respect to the Letter of Intent the muon system has retained the original idea to use the solenoid yoke as muon filter. However the concept design has changed following the results of a preliminary acceptance study and the iron segmentation has been considered for the system optimization.

The momentum range of the DY muons reaching the barrel extends up to few GeV/c. The lower end of the range is fixed by the energy losses and the magnetic bending in the inner detectors (500 MeV/c).

The DY muons crossing the forward endcap show an energy range going from 1 to 3 GeV, with an average energy loss of 250 MeV before to enter the muon counters. The energy of the muons travelling through the Forward spectrometer can be greater than 10 GeV. *here relevant plots* As a consequence slow muons, mainly produced in transverse direction cannot reach the muon system and must be identified by the inner detector. Medium and high energy muons are identified by the muon system only if they are positively detected by the muon detectors and properly match a charged primary track detected by the central tracker. The muon detector output that can be considered for identification purposes is the hit multiplicity in a selected region and, for isolated tracks, a direction and, where possible, a momentum measurement. Range measurement was also suggested as an effective tool for μ/π separation and the arrangement presently under simulation is conceived for this purpose, see fig. 25 and fig. 26.

The following plots show the behaviour of some parameters useful for the muon identification.

The background coming from primary hadrons (mostly pions) could be rejected by the evaluation of the number of planes in the muon system crossed by the charged particle (see fig. for muon and pion of equal energy).

The contamination coming from secondary muons produced by the pion decay could be reduced by considering the angular correlation between the track extrapolated from the vertex and the track segment measured by the muon detectors. In this case (see fig. 27) the measurement of the track momentum by the muon detectors could help.

here(relevant plots
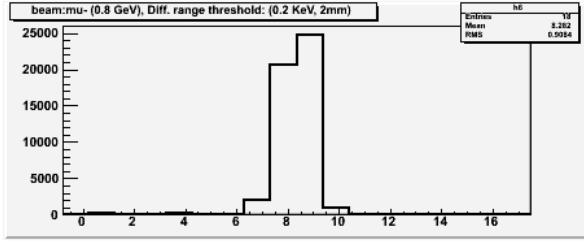
Figure 25: *Range measured as number of crossed planes for a muon with 0.8 GeV energy.*
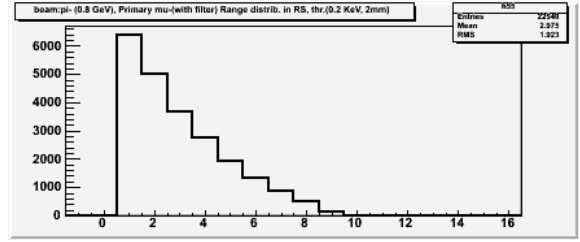
Figure 26: *Range measured as number of crossed planes for a pion with 0.8 GeV energy.*
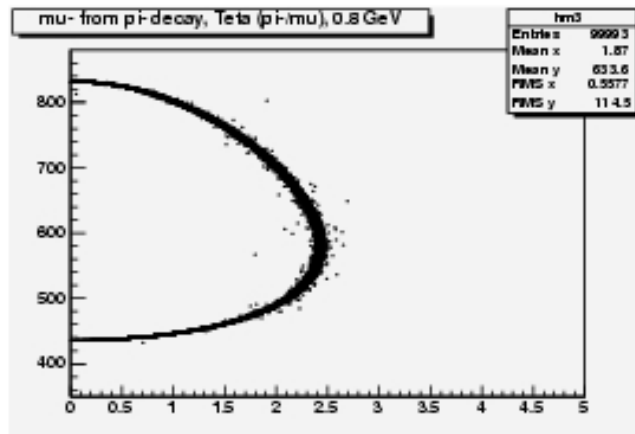
Figure 27: *Muon from decaying pion with 0.8 GeV energy: energy vs decay angle in the Lab system.*

3.7.1 Muon system overview

The parameters considered in the choice of the muon detectors are the spatial and time resolution, to allow independent reconstruction of the track segment direction, the simplicity and flexibility of the design, since the area to be covered is large and divided in different shapes, the robustness the reliability, also in terms of ageing and finally the cost. the MDT have been proven to be a mature and widely used technique that join a very high detection efficiency ($\approx 95\%$) to a great semplicity of production, construction and operation. Following the proposal of thye JINR-Dubna group an eight-cell module of MDT is constituted by a metallic cathode extruded with a comb-like profile and covered by a stainless steel cover. The signal wires pitch is 10 mm, the thickness of the profile is ≥ 0.45 mm and gives the main contribution to the inefficiency of the counter. *here the MDT cross section and the table of the performances*

The MDT are one-coordinate detectors and minimum two layers must be installed to get a track space point. An R&D project is going on at JINR Laboratories aiming to use MDT as two-coordinate detector. For this purpose the stainless steel cover should be removed and substituted by a plastic support for strips or pads. In this case the second coordinate is obtainted by reading out the induced signal.

The MDT are operated in proportional mode. Both the Yes/No readout or the wires and drift

805

Fe (30 mm x 16 layers+ 5 mm x 1 layer)

MDT (20 mm)
(16 layers)
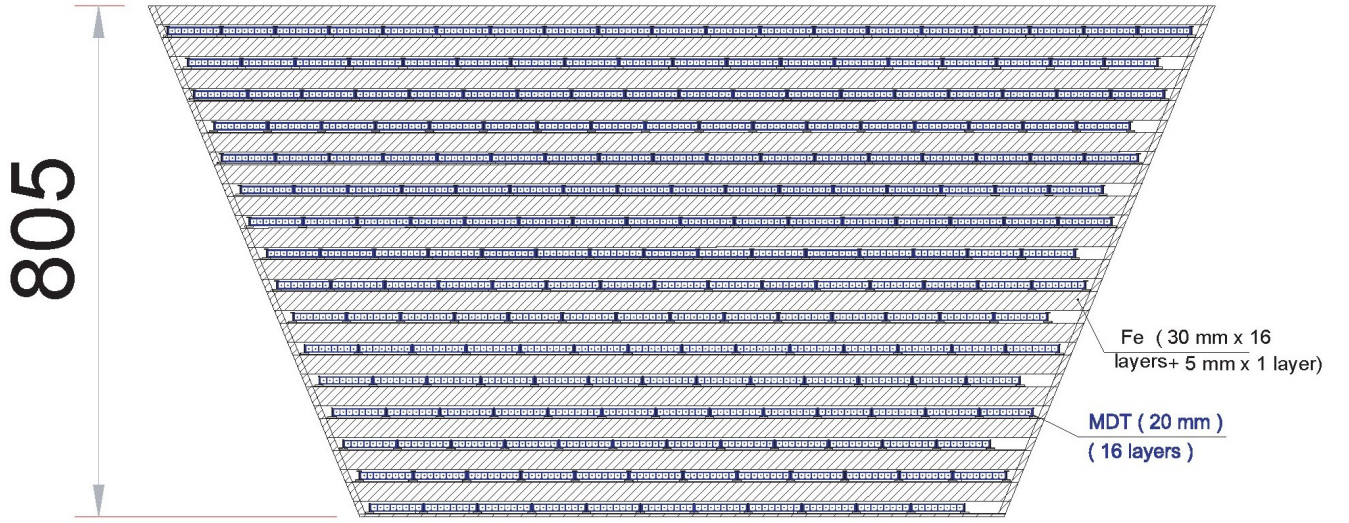
Figure 28: *Cross section of the Muon range system in the Target Spectrometer.*

time measurement are considered for the PANDA operation. The best spatial resolution is obtained in drift mode operation, corresponding to 0.5-0.8 mm r.m.s.

The detector coverage presently considered corresponds to a full coverage of the Target Spectrometer in the trasverse direction with respect to the beam axis (Barrel) and in the forward direction (Forward Endcap), using the yoke of the solenoid as a muon filter. One of the eight parts of the barrel will be only partially covered by muon counters to allow the insertion and the operation of the target and its services. In the Forward Spectrometer (angular coverage from $5° - 10°$ to $0°$ thehadronic calorimeter could be equipped with muon counters.

4   Tools

In this section the TAG work is described. To evaluate the performance of the detectors the PID TAG defined the "Separation Power" as the right tool (see section 4.1. With the help "Phase Space Plots" (section 4.2) the angular coverage and the coresponding particle momenta could be determined. The "Fast Simulation" (section 4.3) was used to map the separation power over the full angular and momentum range. In a second step important reactions and their relevant background channels were simulated. Thus the regions where a good separation power is needed could be identified and checked whether the detector performance is sufficient there.

4.1 Separation Power

This document completely deals with the quality of the particle identification of the projected PANDA detector. Thus the major issue upon which decisions can be made is a proper definition of classification quality or performance.

The according concept chosen for that purpose called 'Separation Power' bases on the assumption that the particular observables of objects of different classes exhibit more or less gaussian distributions.

Consider the situation illustrated in fig. 29.
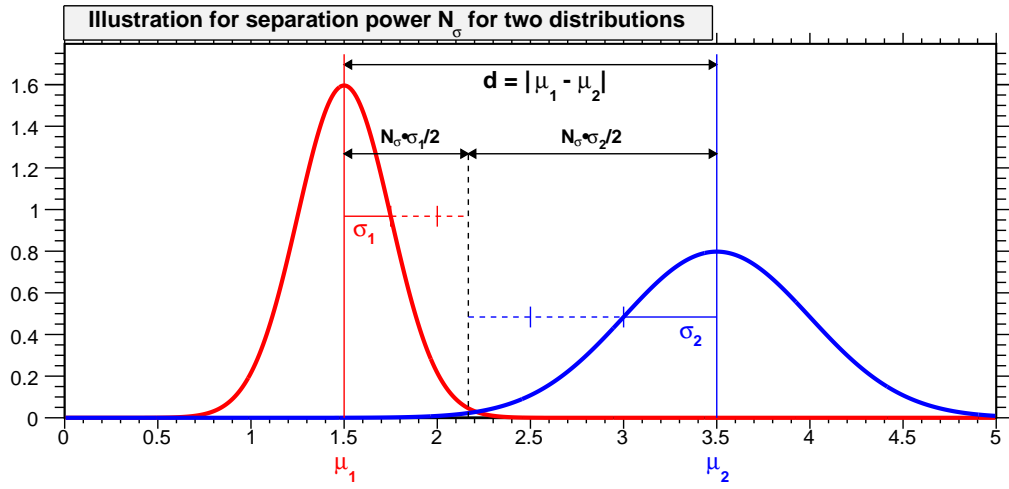
Figure 29: Illustration for the definition of separation power.

There are plotted two gaussian distributions $G_1(x) \equiv G(x; \mu_1, \sigma_1)$ and $G_2(x) \equiv G(x; \mu_2, \sigma_2)$ with mean values $\mu_1 = 1.5$ and $\mu_2 = 3.5$ and standard deviations $\sigma_1 = 0.25$ and $\sigma_2 = 0.5$. This could be e. g. the probability density distributions of the dE/dx measurements for two particle species in a small momentum range. Obviously the distributions are separable quite reasonable, but what is the measure for the separation potential?

A proper definition would be to define a particular classificator, e.g. every particle with property $x_0 < 2$ is considered as member of class 1 (red). Then one can determine two quantities which are of relevance for the qualtity of classification. The first one ist the efficiency, which is part of the distribution 1 (or a random sample of measurements following this distribution) which is identified correctly analytically corresponding to the integral

$$\epsilon = \int_{-\infty}^{x_0} G_1(x)\, dx \tag{1}$$

for a normalized Gaussian. The second quantity is the misidentification level given by the integral

$$\text{mis-id} = \int_{-\infty}^{x_0} G_2(x)\, dx \tag{2}$$

which is part of the distribution 2 in the same region thus identified incorrectly as being of class

1. These two values would define clearly the performance of the classificator[2]. But this solution cannot be applied in case when one does not want to define a particular selector. It rather has to be defined a measure for the prospective performance of a possible selector.

Exactly this is the aim of the separation power N_σ which relates the distance of the mean values $d = |\mu_1 - \mu_2|$ of the two distributions to their standard deviations σ_1 and σ_2. The usual unit of N_σ is 'number of gaussian sigmas of the separation potential', which is supposed to relate the number with gaussian integral values.

There are actually a lot of different definitions for that quantity on the market but it has been found an agreement within the PID TAG on the following definition:

$$N_\sigma = \frac{|m_1 - m_2|}{\sigma_\beta} = \frac{|m_1 - m_2|}{(\sigma_1/2 + \sigma_2/2)} \tag{3}$$

This relationship is illustrated in fig. 29. The black dashed line marks the position x_0 between the two distributions, for which the differences to each mean value $|m_1 - x_0| = N_\sigma \cdot \sigma_1/2$ and $|m_2 - x_0| = N_\sigma \cdot \sigma_2/2$ are the same in terms of σ's.

This means a separation of e. g. $N_\sigma = 4\sigma$ corresponds to a gaussian integral

$$I = \int_{-\infty}^{\mu+4\sigma/2} G(x; \mu, \sigma)\, dx = 0.9772 \tag{4}$$

which shall express an efficiency around $\epsilon \approx 97.7\%$ or a mis-ID level around mis$=100\% - 97.7\% \approx 2.3\%$ or both. This integration up to half the number of sigmas $N_\sigma/2$ seems a bit contra intuitive but is common notion and therefore has kept for the considerations in this document. Another feature of this definition is that it is symmetric for both classes or distributions, even with different σ's. Furthermore for the particular case of normalized gaussian distributions and a selector requiring $x < x_0$ for classifying class 1 objects in the upper example, the efficiency ϵ and purity π for this selection have the same value, since

$$\epsilon = \frac{\int_{-\infty}^{x_0} G_1(x)\, dx}{\int_{-\infty}^{+\infty} G_1(x)\, dx} = \frac{\int_{-\infty}^{x_0} G_1(x)\, dx}{1} = \frac{\int_{-\infty}^{x_0} G_1(x)\, dx}{\int_{-\infty}^{x_0} G_1(x)\, dx + \int_{x_0}^{+\infty} G_1(x)\, dx} \tag{5}$$

$$= \frac{\int_{-\infty}^{x_0} G_1(x)\, dx}{\int_{-\infty}^{x_0} G_1(x)\, dx + \int_{-\infty}^{x_0} G_2(x)\, dx} = \frac{\int_{-\infty}^{x_0} G_1(x)\, dx}{\int_{-\infty}^{x_0} G_1(x) + G_2(x)\, dx} = \pi \tag{6}$$

Tab. 3 lists on the left hand side the mis-id levels $1 - \int G(x)dx$ with 1-sided and 2-sided gaussian integrals for different values of N_σ, on the right hand side the corresponding values of the separation power for given levels of mis-id according to the upper definition. It shall be emphasized again that for given values N_σ the integration is only performed up to $N_\sigma/2$, therefore the mis-id levels might seem surprisingly high for given number of σ's separation.

Taking into account that quantities in reality never have gaussian shape the values σ in fact are not necessarily gaussian sigmas but calculated as the root-mean-square (which actually is the standard deviation)

$$\sigma_{\mathrm{rms}} = \sqrt{\sum_i (x_i - \mu)^2} \tag{7}$$

---

[2]For Bayes' classification a flux correction would have to be taken into account additionally. This requires of course knowledge about a posteriori probabilities of particle fluxes which not necessarily is available since significantly dependent on the given trigger and reaction type.

528 what in case of gaussian distribution would be indeed identical with the gaussian σ from above.
529 For the given example in fig. 29 the definition (3) computes to

$$N_{\sigma,1} = \frac{2}{0.25/2 + 0.5/2}\,\sigma = \frac{2}{0.375}\,\sigma = 5.333\,\sigma \quad .$$

530 Another issue with directly is connected with the upper definition is the question how to define
531 the combined separation $N_{\sigma,\text{tot}}$ e.g. for values $N_{\sigma,i}$ achieved by various detector components to
532 express the overall performance. The agreement of the PID-TAG concerning this was to consider
533 the quadratic sum

$$N_{\sigma,\text{tot}} := \left(\sum_i N_{\sigma,i}^2 \right)^{1/2} \tag{8}$$

534 as a good measure. In order to evaluate the goodness of that expression it first of all is necessary to
535 make aware what meaning the value N_σ has in terms of probablity. When considering something
536 similar to equation (4) as a appropriate measure, namely the integral of a Gaussian from $-N_\sigma/2$
537 to $+N_\sigma/2$ the expression for the corresponding probability of mis-identification is given by

$$P_{\text{mis}}(N_\sigma) = 1 - \int_{-N_\sigma/2}^{+N_\sigma/2} G(x; \mu = 0, \sigma = 1)\,dx \tag{9}$$

538 which directly defines the mis-identification probability for n statistically independent separation
539 capabilities as the product

$$P_{\text{mis,tot}} = P_{\text{mis}}(N_{\sigma,1}) \times \cdots \times P_{\text{mis}}(N_{\sigma,n}) \tag{10}$$

540 in addition. Hence equation (9) implicitly specifies $N_{\sigma,\text{tot}}$ as that value where the intergral yields
541 exactly $P_{\text{mis,tot}}$. This procedure has been pursued for two values $N_{\sigma,1}$ and $N_{\sigma,2}$ as presented in fig.
542 30. In (a) the combined separation power is shown as 2-dimensional function of the two input
543 values, (b) presents the difference

$$\Delta = \left| N_{\sigma,\text{tot}} - \sqrt{N_{\sigma,1}^2 + N_{\sigma,2}^2} \right| \tag{11}$$

544 of the resulting value and equation (8), which obviously reasonably reproduces the correct value
545 with a maximum deviation of about 0.5σ in the range of single values up to $N_\sigma = 6$.

4.1.1   Parametrization of the Electromagentic Calorimeter

547 Although not implemented in the Fast Simulation, a parametrization of part of the response
548 of the EMC has been persued for the estimation of overall PID quality. It is based on fully
549 simulated data but only information about electron-pion-separation was taken into account up to
550 now. Fig. 31 (a) shows the distributions of the parametrized ratio of the calibrated cluster energy
551 in the electromagnetic calorimeter and the reconstructed track momentum E_{clus}/p for simulated
552 electrons (green) and pions (black). The source for modelling the parametrizations can be found
553 in the PANDA Physics Book [?]. It is clearly visible that above momenta of approximately 500
554 MeV this quantity is a powerful tool to separate electrons from pions, demonstrated in fig.31 (b),
555 where the separation power has been determined dependend of the track momentum p by the
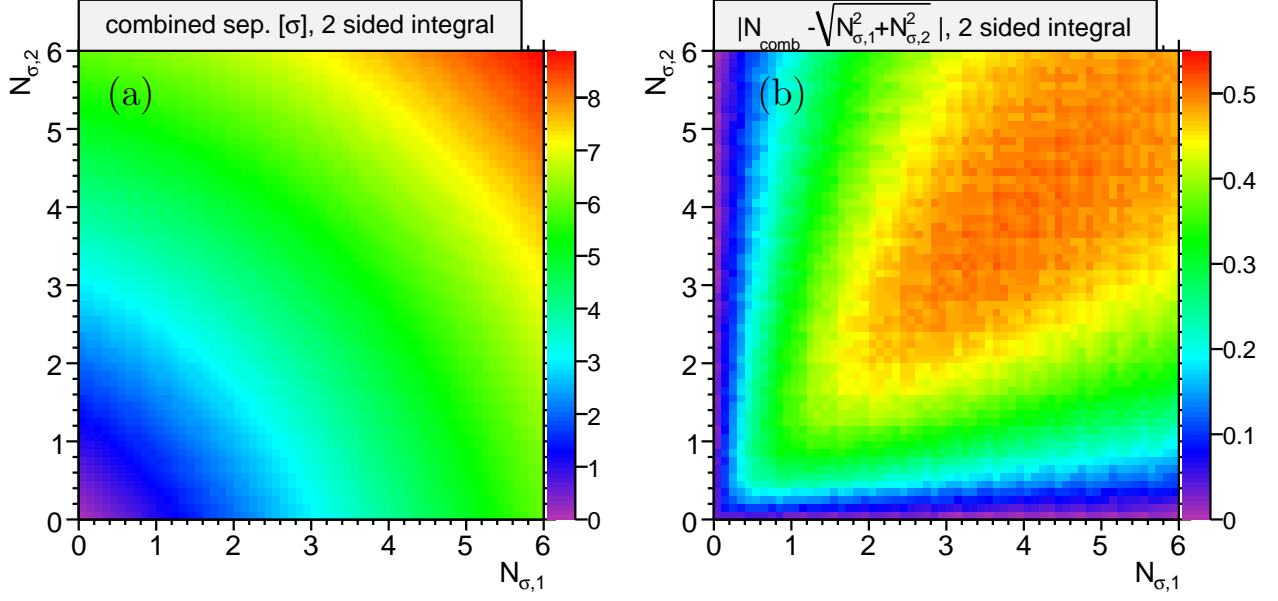
Figure 30: (a) Graphical representation of the combined separation power $N_{\sigma,\text{tot}}$ of two values $N_{\sigma,1}$ and $N_{\sigma,2}$, (b) the corresponding difference $\left| N_{\sigma,\text{tot}} - \sqrt{N_{\sigma,1}^2 + N_{\sigma,2}^2} \right|$.

N_σ	mis-id (1s) [%]	mis-id (2s) [%]	mis-id [%]	N_σ (1s)	N_σ (2s)
1.0	30.854	61.708	10.000	2.6	3.3
2.0	15.769	31.538	5.000	3.3	3.9
3.0	6.681	13.361	1.000	4.6	5.1
4.0	2.254	4.507	0.500	5.1	5.6
5.0	0.621	1.242	0.100	6.2	6.6
6.0	0.133	0.266	0.050	6.6	7.0
7.0	0.023	0.047	0.010	7.4	7.8
8.0	0.003	0.006	0.005	7.8	8.1
9.0	0.000	0.001	0.001	8.5	8.8

Table 3: Relation between separation power and mis-id level

definitions given above. Since no θ dependence was available this separation power is assumed to be constant over the complete θ range.

According to the software chapter of the PANDA Physics Book e/π separation is the most difficult one. Therefore this distribution is assumed to also hold for separating electrons from any other particle species.

As a very naive assumption without a proof the additional separation power provided by the EMC for any other particle combination is taken to be 1σ over the complete phase space covered by the EMC.
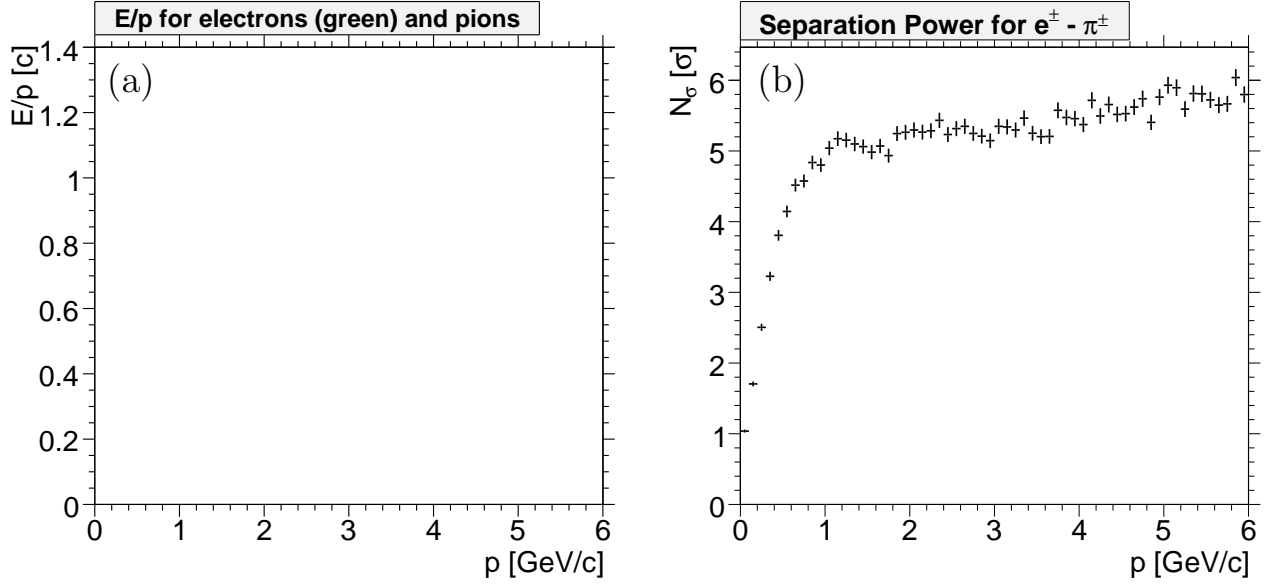
Figure 31: (a) Parameterized distribution of E_{clus}/p for electrons and pions and (b) the resulting separation power N_σ as function of the track momentum p.

4.1.2   Mapping Separation Power

For the purpose of illustration the relationship between kinematic distributions of physics channels and the PID quality the separation power defined in (3) has been determined as 2-dimensional histogram in phase space (p, θ). Therefore it was necessary to computed the mean value μ and standard deviation σ for every bin i with $[p_i \ldots p_i + dp; \theta_i \ldots \theta_i + d\theta]$ for bin widths dp and $d\theta$ for every detector and particle species.

One technical remark: To avoid the computation of $(x - \mu)$ for every measurement in order to determine σ, which is very time consuming for large datasets, the relationship

$$\sigma = \frac{1}{N}\sqrt{\sum x_i^2 - \left(\sum x_i\right)^2} \tag{12}$$

has been exploited which does not require a previous calculation of the mean value $\mu = \bar{x}$.

In order to evaluate the contributions of the various detectors to the overall classification potential, the separation power defined above has been determined for every single detector component and all possible particle combinations, which add up to the following 10 possibilies:

1. $e^\pm - \mu^\pm$, $e^\pm - \pi^\pm$, $e^\pm - K^\pm$, $e^\pm - p/\bar{p}$,

2. $\mu^\pm - \pi^\pm$, $\mu^\pm - K^\pm$, $\mu^\pm - p/\bar{p}$,

3. $\pi^\pm - K^\pm$, $\pi^\pm - p/\bar{p}$,

4. $K^\pm - p/\bar{p}$.

The results are determined based upon 5 million isotropic distributed single track events with particle momenta up to 6 GeV/c.

Figs. 32 and 34 show as examples the p–θ–dependent separation power for $e^{\pm} - \pi^{\pm}$, $\pi^{\pm} - K^{\pm}$ and $K^{\pm} - p/\bar{p}$ for all 8 detector components

- Micro Vertex Detector (MVD)

- Barrel Time of Flight System (TOF)

- Barrel DIRC

- Disc DIRC

- Ring Image Cherenkov Detector (RICH)

- Electro Magnetic Calorimeter (EMC)

- Straw Tube Tracker (STT)

- Time Projection Chamber (TPC)

under investigation. The color codes in these 2 dimensional representations correspond to the numbers of σ's N_σ of separation with a cutoff $N_\sigma > 8$, so in the red regions are possibly values above that limit.

To get an impression of the overall particle identification performance the values $N_{\sigma,i}$ from the different detectors i have been combined by quadratic summation according to (8) under the assumption of statistically uncorrelated $N_{\sigma,i}$. Since there are two central tacker options (STT and TPC) which cannot contribute to the same total separation, two different scenarios with either the STT or the TPC are considered separately. Fig. 35 shows the combined information for the STT option and fig. 36 for the detector setup with the TPC as central tracker. All maps are based on the requirement of positiv identification of a particle species. This means, that particle type A is only considered to be dsitinguishable from another particle type B when both create a signal in the particular detector and the given phase space region.

One should keep in mind that the conclusive power of separations involving electrons and muons is limited for the time being since only limited information from the electromagnetic calorimeters and none for the muon detectors has been incorporated so far, which has significant impact on electron and muon identification respectively.
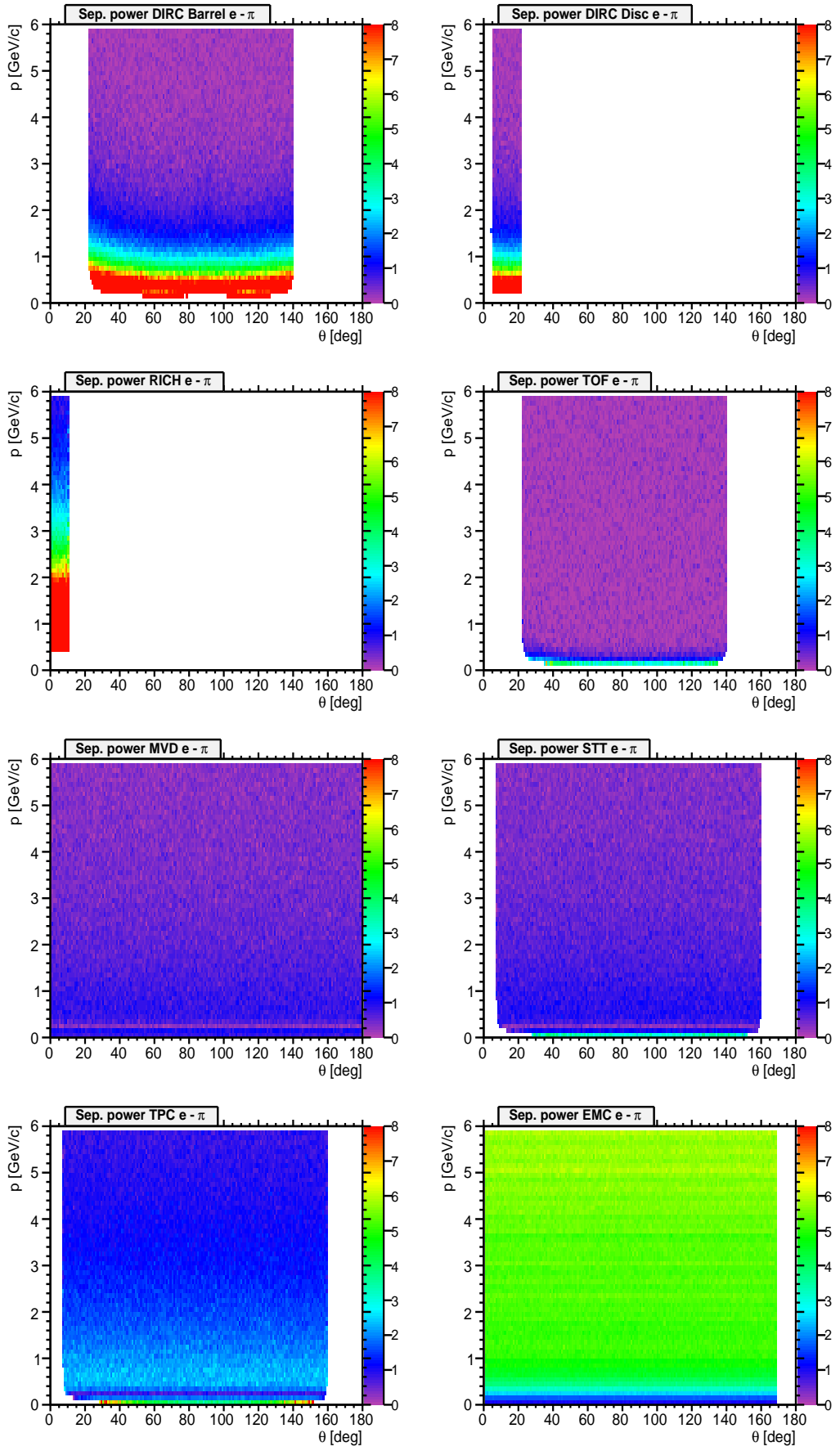
Figure 32: Map of separation power for $e^{\pm}$–$\pi^{\pm}$ separation. Color code corresponds to $N_{\sigma} = 0 \ldots 8$.
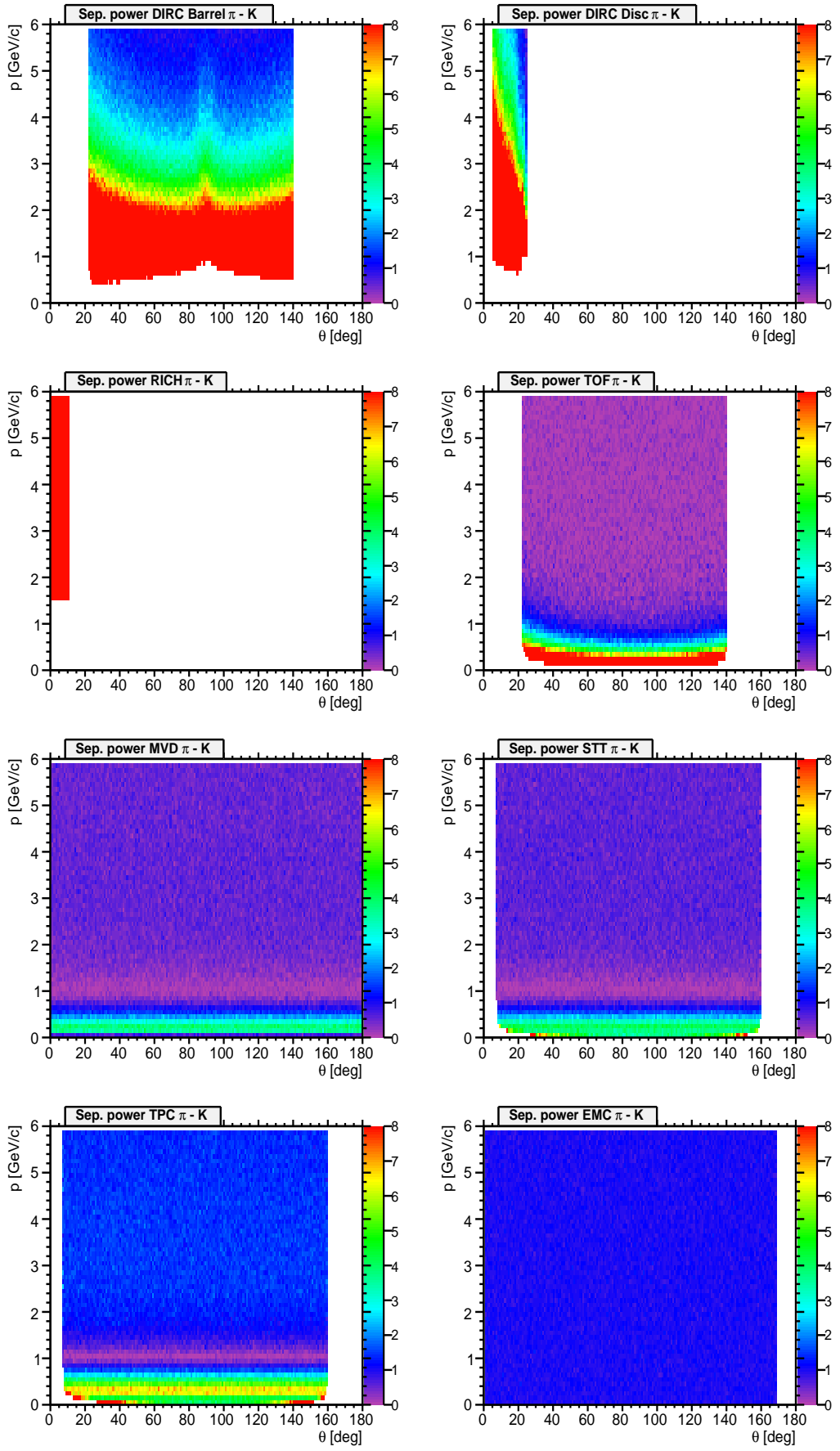
Figure 33: Map of separation power for $\pi^{\pm}$–$K^{\pm}$ separation. Color code corresponds to $N_{\sigma} = 0 \ldots 8$.
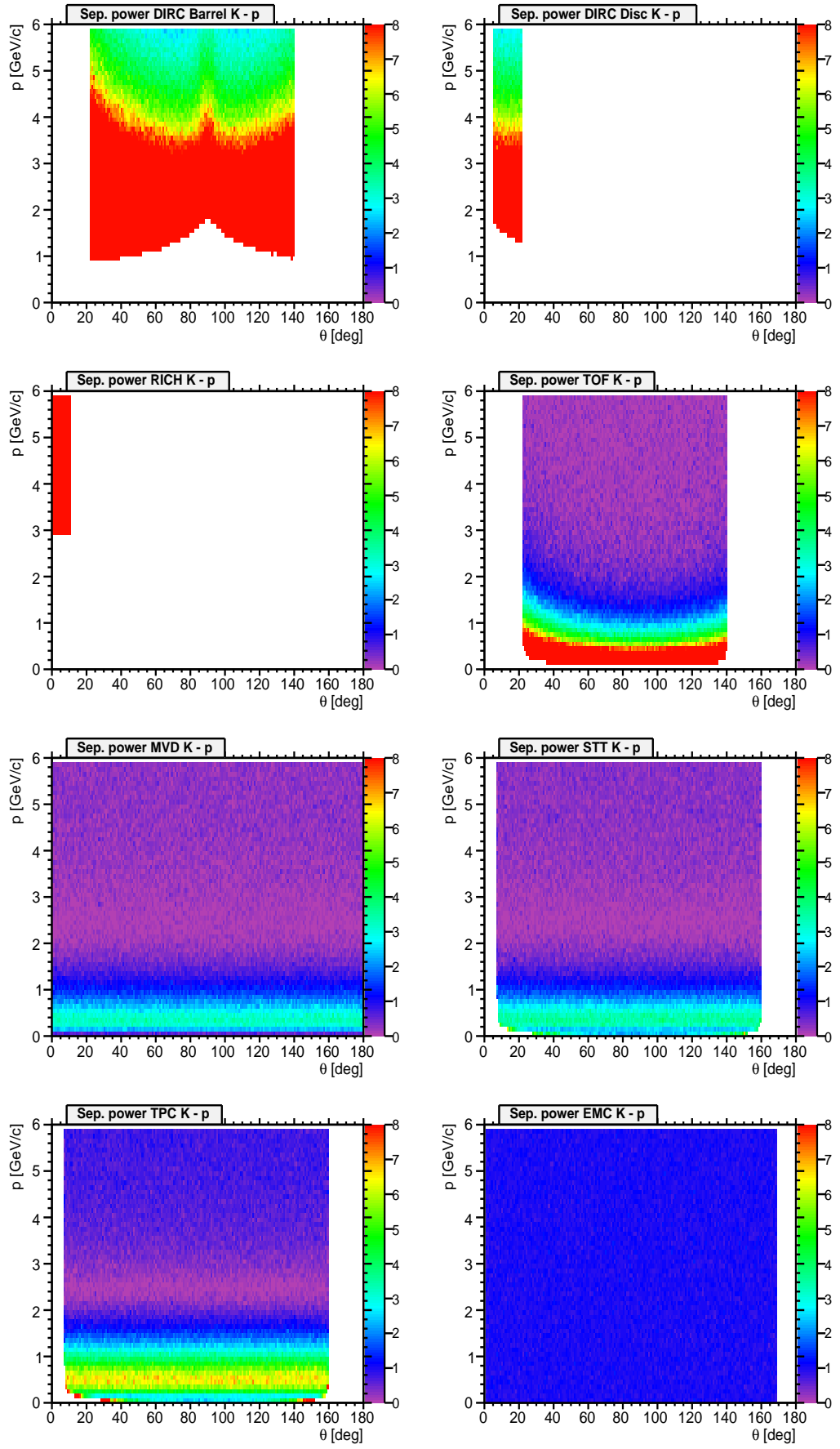
Figure 34: Map of separation power for $K^{\pm}$–$p/\bar{p}$ separation. Color code corresponds to $N_\sigma = 0 \ldots 8$.

Figure 35: Combined map of Separation Power with STT as central tracker option including the TOF system. Color code corresponds to $N_\sigma = 0 \ldots 8$.
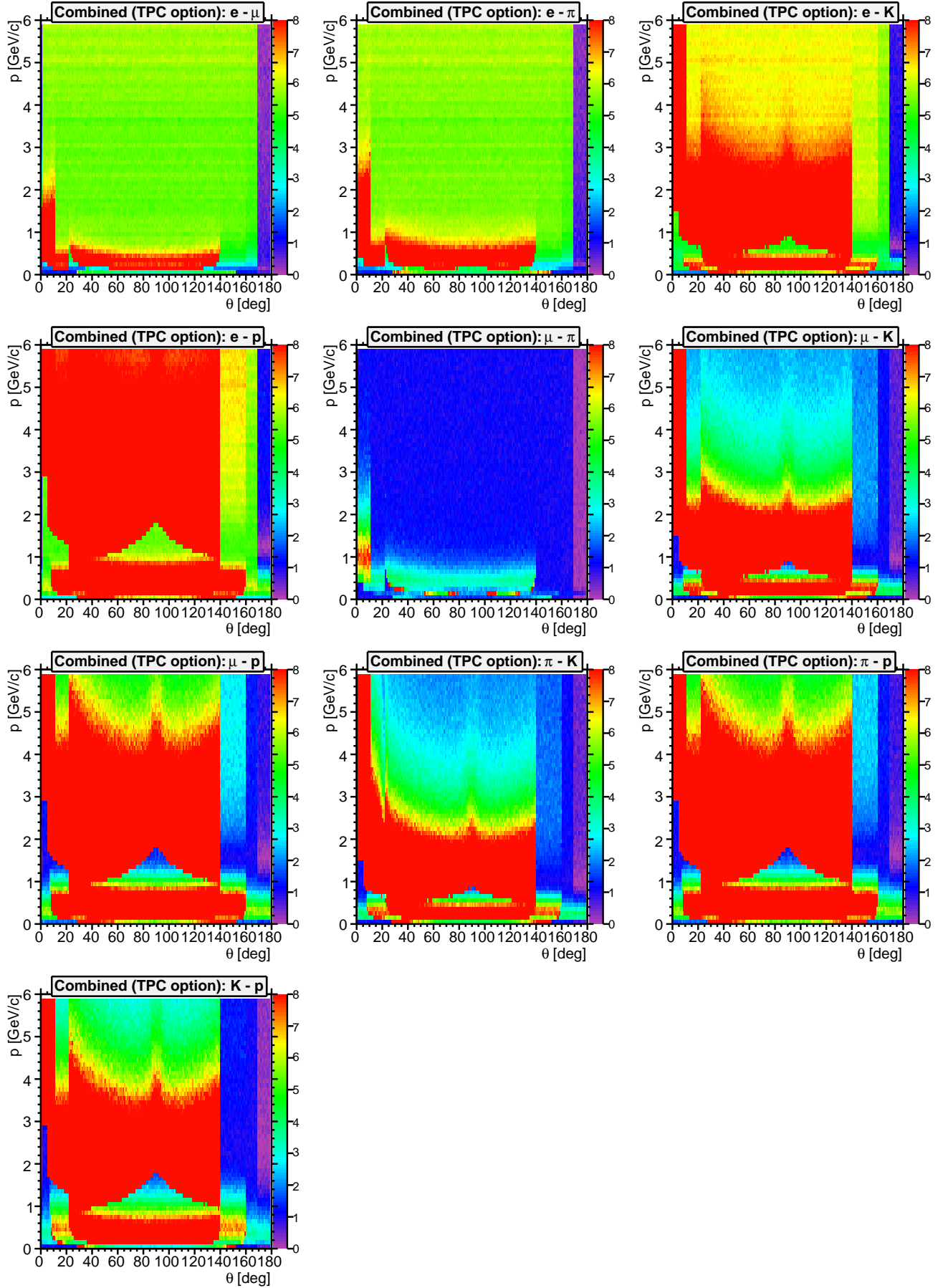
Figure 36: Combined map of Separation Power with TPC as central tracker option including the TOF system. Color code corresponds to $N_\sigma = 0 \ldots 8$.
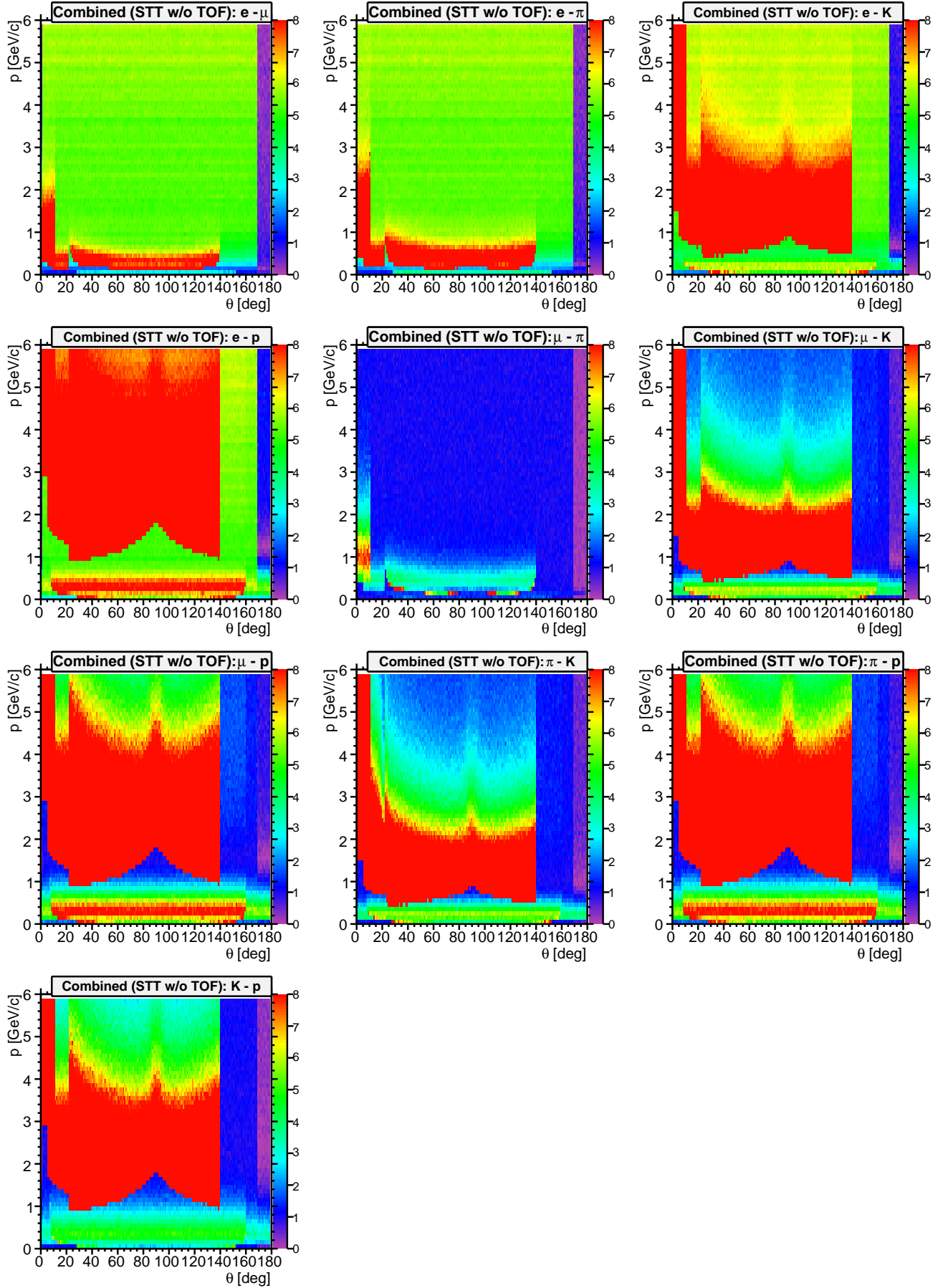
Figure 37: Combined map of Separation Power with STT as central tracker option without the TOF system. Color code corresponds to $N_\sigma = 0 \ldots 8$.
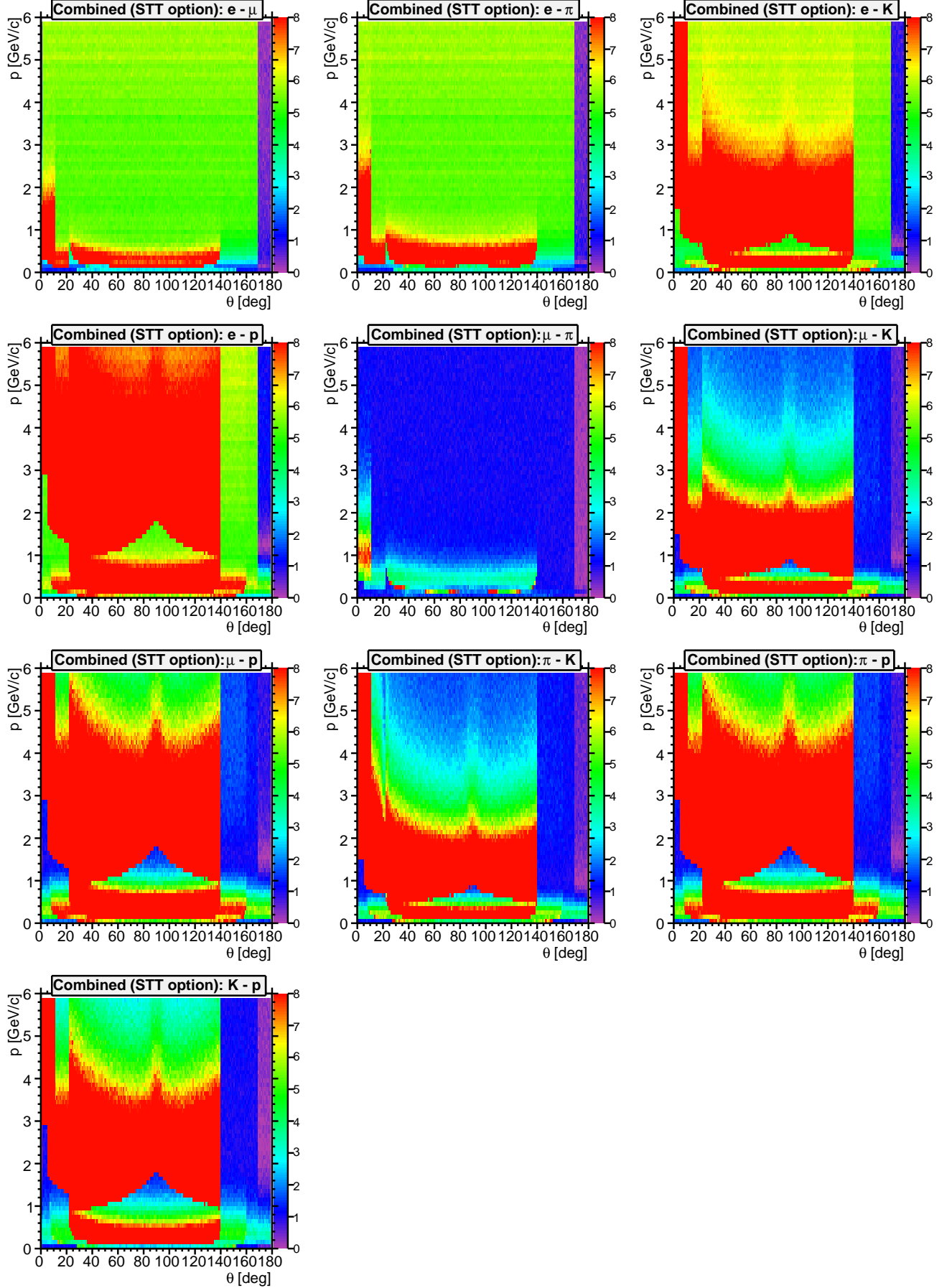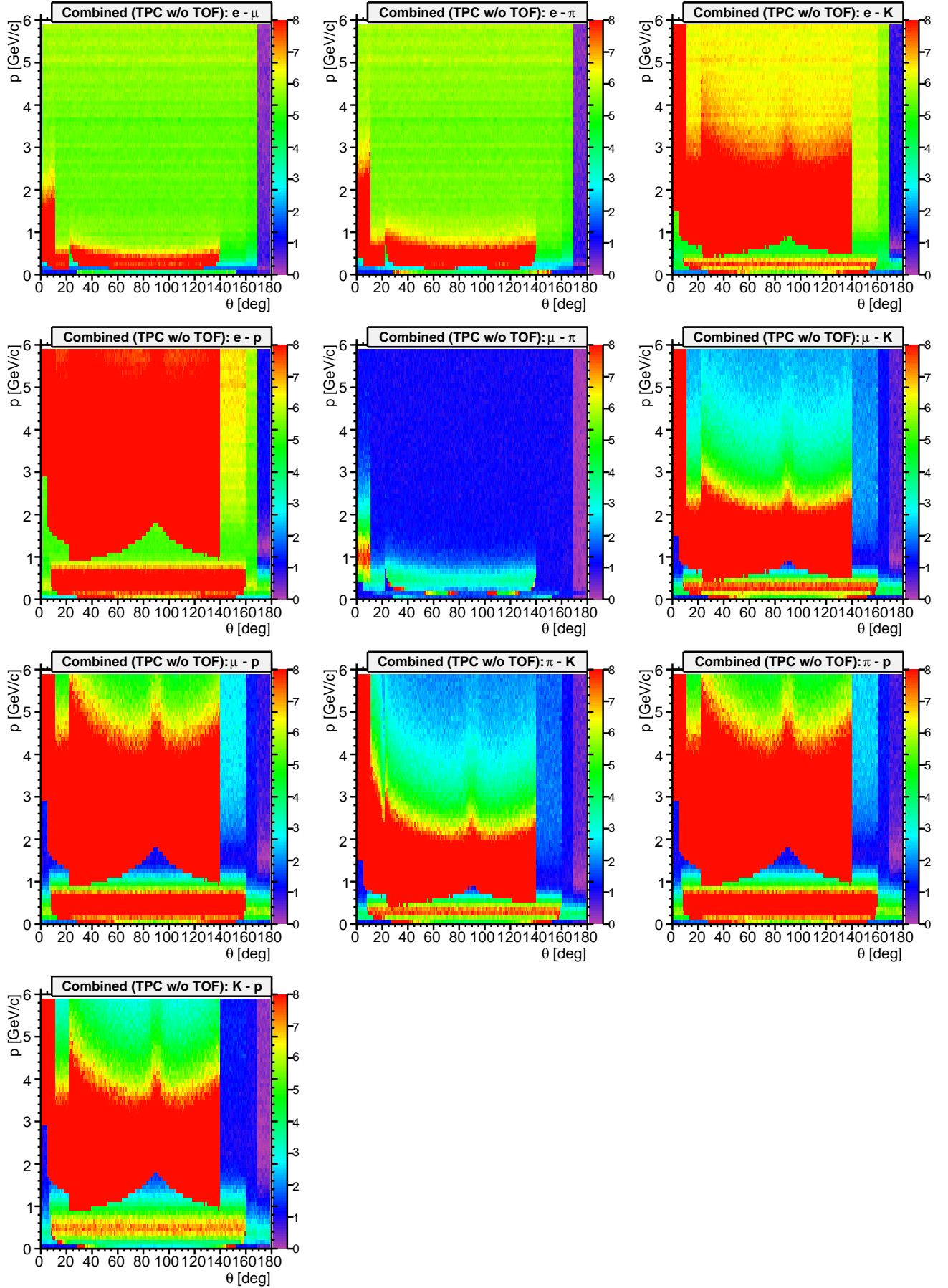
Figure 38: Combined map of Separation Power with TPC as central tracker option without the TOF system. Color code corresponds to $N_\sigma = 0 \ldots 8$.

4.2   Phase Space Plots

The question which has to be answered concerning particle identification is not only how good the classification works or has to work, but also in which region of the phase space one needs good separation, and in which parts one possibly doesn't need almost any.

Therefore it is a crucial task to visualize the kinematic behaviour of various important physics channels to get a better insight to the above issue. Furthermore not only kinematic distributions of signal events are relevant, since good PID is only useful in cases where kinematic overlap of particles of species A from signal events and particles of species B from background events really exists. In scenarios where particles of the same type A appear in signal as well as background events in the same phase space location the background suppression cannot be improved by means of PID.

Following a request of the PID TAG phase space plots from all the reactions relevant for the physics book were produced. The set of plots shows for each particle species of the reaction the particle momentum versus theta angle.

Tab. 5 lists part of the benchmark channels discussed in the PANDA Physics Booklet and some additional ones to study inclusive open charm analysis together with relevant background channels. In particular channels were investigated which might suffer significantly from insufficient PID capabilities[3].

The acronym DPM in the table refers to generic background evens generated with the **D**ual **P**arton **M**odel generator. In the last column references to the corresponding figures are given. Tab. 4 gives some standard decay channels which apply to cases where nothing different is specified in tab. 5.

In figs. 39 - 43 kinematic distributions (momentum p vs. dip angle θ) at various beam momenta are shown for some of the signal-background scenarios listed in 5, one particle species per plot. To easier spot signal and background, the latter ones are colored blue.

Particle	Decay channel
J/ψ	50% e^+e^-, 50% $\mu^+\mu^-$
η	$\pi^+\pi^-\pi^0$
D^0	$K^-\pi^+$
D^+	$K^-\pi^+\pi^+$
D^{*+}	50% $D^0\pi^+$, 50% $D^+\pi^0$
D^{*0}	$D^0\pi^0$
D_s^+	$\phi\pi^+$
ϕ	K^+K^-
Λ	$p\pi^-$
π^0	$\gamma\gamma$

Table 4: Standard decay channels for some particles

---

[3]Signal channels with background reactions comprising the same final state can only be identified due to different kinematic behaviour, which goes beyond the capabilities of PID
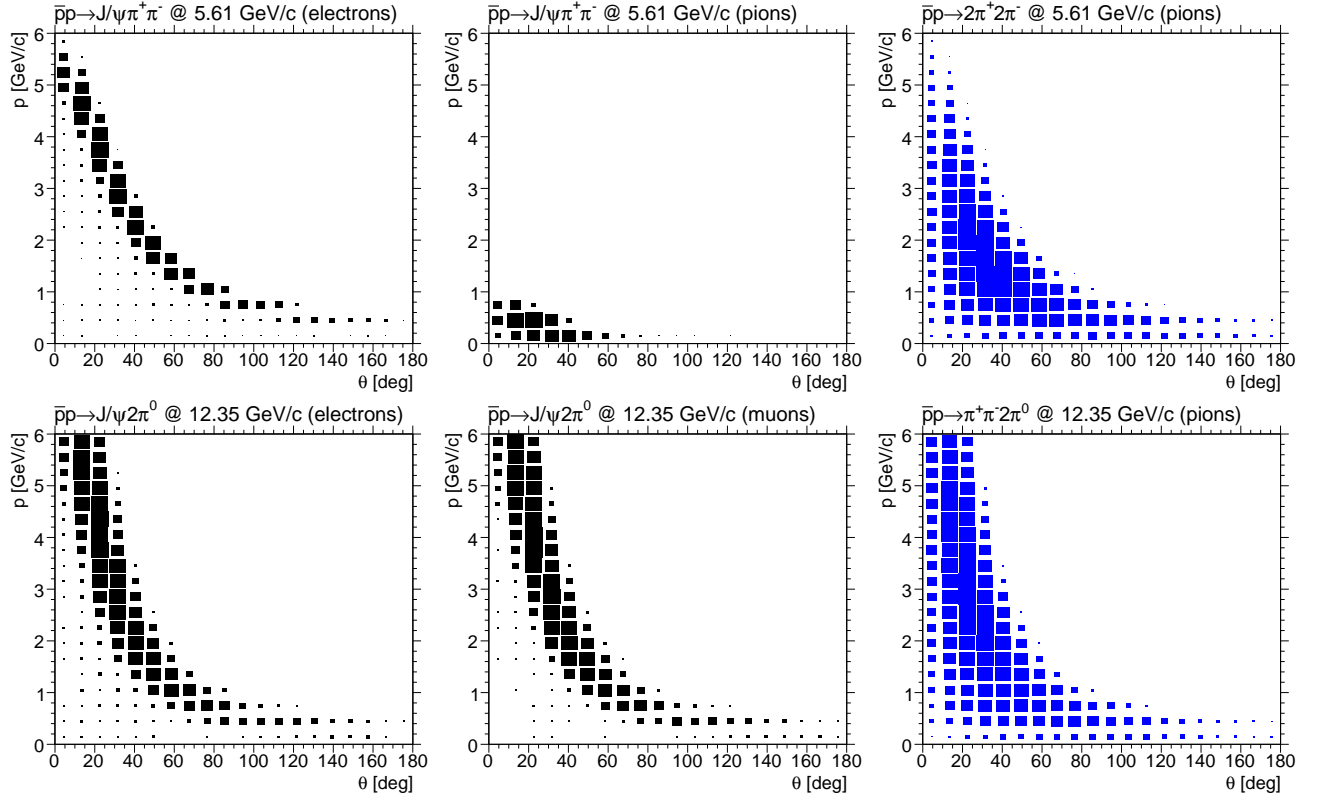
Figure 39: $\bar{p}p \rightarrow J/\psi\pi^+\pi^-$ @ 5.609 GeV/c (top), $\bar{p}p \rightarrow J/\psi 2\pi^0$ @ 12.3485 GeV/c (bottom)
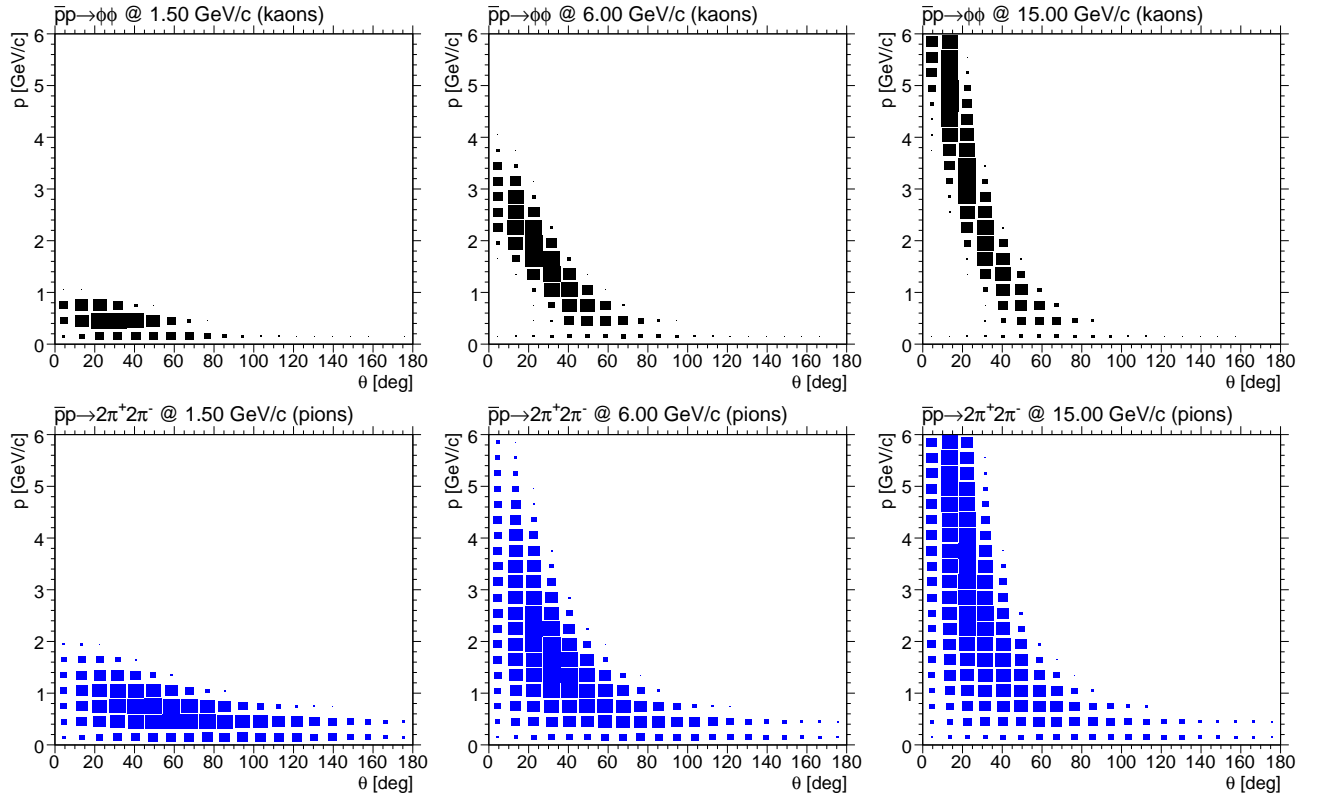
Figure 40: $\bar{p}p \rightarrow \phi\phi$ @ 1.5, 6.0, 15.0 GeV/c
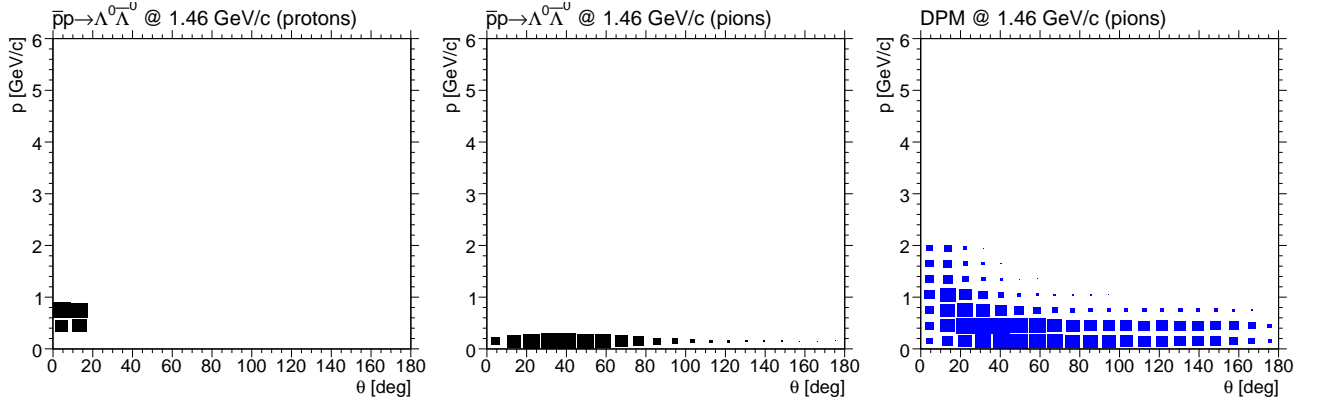
Figure 41: $\bar{p}p \to \Lambda^0\bar{\Lambda}^0$ @ 1.4601 GeV/c
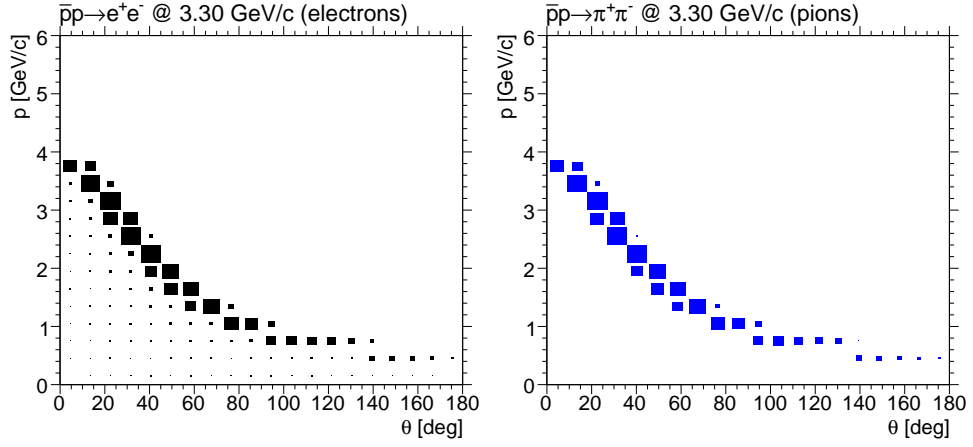
Figure 42: $\bar{p}p \to e^+e^-$ @ 3.30 GeV/c
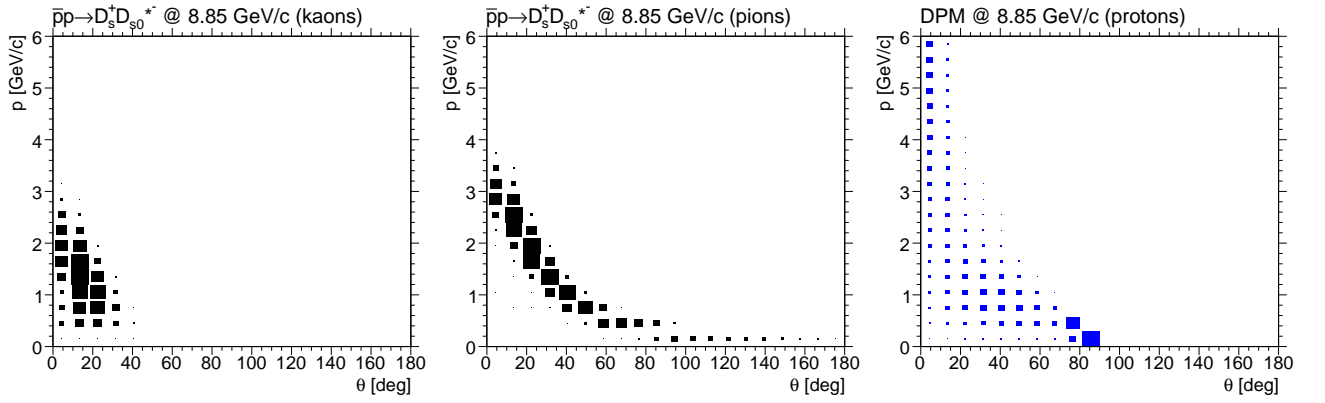
Figure 43: $\bar{p}p \to D_s^+ D_{s0}^*(2317)^-$ @ 8.847 GeV/c

Signal	Background	$p_{\bar{p}}$ [GeV/c]	Fig.
$J/\psi 2\pi^0$	$\pi^+\pi^- 2\pi^0$	5.609 / 6.232 /8.682	
		10.295 / 12.349	39
$J/\psi\pi^+\pi^-$	$2\pi^+2\pi^-$	5.609 / 6.232 / 6.988	
		8.682 / 10.295 / 12.349	-
	$2\pi^+2\pi^-\pi^0$	6.990 / 8.7	-
$J/\psi\eta$	$2\pi^+2\pi^-$	6.080 / 6.990 / 8.7	-
	$3\pi^+3\pi^-$	6.080 / 6.990 / 8.7	-
$\phi\phi$	$2\pi^+2\pi^-$	1.5 / 6.0 / 12.0 / 15.0	40
	$3\pi^+3\pi^-$	1.5 / 6.0 / 12.0 / 15.0	-
$\Lambda^0\bar{\Lambda}^0$	$\Sigma^0\bar{\Sigma}^0$	1.914 / 3.101 / 6.0	41
	DPM	1.460 / 8.0 / 10.0	-
e^+e^-	$\pi^+\pi^-$	1.7 / 3.3 / 7.9 / 10.9 / 15.0	42
$D_s^+ D_{s0}^*(2317)^-$	DPM	8.847	43
	$3\pi^+3\pi^-\pi^0$	8.847	-
$D_s^+ D_s^- \gamma$	$3\pi^+3\pi^-$	8.847	-
	DPM	7.361 / 7.746 / 8.0 / 12.0 / 15.0	-
$D^{*0}\bar{D}^{*0}\gamma$	DPM	7.746 / 8.0 / 12.0 / 15.0	-
$D^{*+}D^{*-}\gamma$	DPM	7.746 / 8.0 / 12.0 / 15.0	-
$D^0\bar{D}^0\gamma$	DPM	6.488 / 8.0 / 12.0 / 15.0	-
$D^+D^-\gamma$	DPM	6.488 / 8.0 / 12.0 / 15.0	-

Table 5: Table of Phase Space Channels

4.3   Fast Simulation

In order to get information about phase space (i.e. momentum-polar angle dependence) coverage of the different PID relevant subsystems maps of separation power have been generated based on fast simulations of single track events, i.e. the particles properties are modified with an effective parametrization of detectors responses and PID information is estimated and attached to the resulting particle candidate. Since no microscopic simulation is performed and no exact geometry information is taken into account, the accuracy of this approach is limited, the computation time on the other hand is orders of magnitude shorter offering the possibility to do studies with higher statistics.

4.4   General Technique

In contrast to microscopic simulations using software systems like Geant or Fluka the Fast Simulation is based on acceptance filtering and effective parametrization of all observables of the particular subsystems. Underlying assumption is that the detector system will be able to recontruct the true particles properties like momentum, direction, energy, charge and particle identification (PID) information with uncertainties which are basically uncorrelated and can be described reasonable by parametric models. That could as simple example be gaussian uncertainty for momentum reconstruction with $\delta p/p = \sigma_p = 2\%$, which will be used to modify the true (i.e. generated) tracks parameters accordingly. Additionally a simple geometric accptance requirement will decide whether a track has been detected by a particular detector component or not.

There is a lot of freedom for the implementation of the subsystems, but a minimalistic detector description comprises

- Sensitivity information: Detects charged or neutral particles or both?

- Polar angle coverage: $\theta_{\min} < \theta < \theta_{\min}$

- Gaussian resolution of observables: $\sigma_1, \ldots, \sigma_n$

In order to apply these simulation scheme for every trackable particle coming from the event generator the following procedure is processed:

1. For all detectors D_j, $1 < j < m$

    - In case D_j detects the particle, collect resolution information for all measurable quantities.

2. When no detector detected the track, skip it.

3. Merge all resolution information; when e. g. the particle has been detected by n devices capable of measuring momentum p with resolutions $\sigma_{p,1}, \ldots, \sigma_{p,n}$, the total resolution is

$$\sigma_p = \left(\sum_{i=0}^{n} \frac{1}{\sigma_{p,i}^2} \right)^{-\frac{1}{2}}$$

4. Modify the according quantities x of the original track in the way $x' = x + \delta x$, with δx randomly chosen from gaussian distribution $G(\mu = 0, \sigma_x)$

5. Create PID information according to the particles properties and attach to the particle; add particle to the track list

6. (Optional) Create secondary particles related to particles properties and add to the track list

With the so prepared track list analysis can be performed. The interface for doing that is exactly the same as the one for full simulated events.

Since this document is focussing on PID the relevant features will be describe in more detail in the following chapters. This will be done effect– or observable–wise instead of detector–wise, since the observed quantities

- specific energy loss dE/dx (MVD, TPC, STT)

- Cherenkov angle θ_C (Barrel DIRC, Disc DIRC, RICH)

- reconstructed squared mass m^2 (TOF)

- EMC related measurements like E_{cluster}/p or Zernike momenta

- signals from Muon Chambers

govern the PID quality and performance and thus are a better ordering criterion. Unfortunately the latter two informations from e.-m. calorimetry and the muon detectors are not implemented in the Fast Simulation for the time being.

4.5   Tracking Detectors

Although not of direct impact to the field of PID the process of tracking delivers vital information for many of the PID relevant systems. Most of these like e.g. the Time-of-flight (TOF) system or Cherenkov devices (DIRCs and RICH) do not allow for performing a stand alone position measurement, thus their information have to be linked to tracks reconstructed by tracking devices. In addition for the purpose of evaluating PID likelihood functions one usually needs to compute expected values for observables like the Cherenkov angle θ_C or energy loss dE/dx which will be computed for the reconstructed momentum value of the track. This certainly will differ from the true momentum value and therefore track reconstruction accuracy has important impact on likelihood based classification methods.

The approach for reconstruction of momenta in the Fast Simulation nevertheless is a very simple one assuming a global momentum resolution $\delta p/p$ for the track reconstruction, since due to technical reasons the particular detector components cannot exchange information. This implies that the tracking devices are not able to feed their information into the PID systems.

4.6   Energy Loss Parametrization

The computation of the specific energy loss is based on the Bethe-Bloch formula

$$-\frac{dE}{dx} = \kappa \cdot \frac{Z}{A} \cdot \frac{e^2}{\beta^2} \cdot \left[\ln\left(\frac{2m_e\beta^2\gamma^2 T_{\max}}{I^2}\right) - 2\beta^2 - \delta\right] \qquad \left[\frac{\mathrm{MeV}\cdot\mathrm{cm}}{\mathrm{g}}\right] \tag{13}$$

which very precisely takes into account the processes of charged particles interacting with matter. The formula and detailled information about parameter meanings in this term can be found in [7].

The expression looks quite complicated but can be evaluated straight forward with momentum p and mass m given as input. Additionally one has to substitute a lot of other, material related constants. Since we are not interested in the absolut energy loss but only in relative losses for different particle species it is not crucial to have very precise knowledge about the fixed parameters.

In order to generate a simulated detector response for detectors capable of measuring dE/dx a gaussian resolution $\sigma_{dE/dx}$ has been set for each of them. The simulated measured $(dE/dx)_{\mathrm{sim}}$ value thus has been simply computed with formula (13) to

$$\left(\frac{dE}{dx}\right)_{\mathrm{sim}} = \left(\frac{dE}{dx}\right) + \delta\left(\frac{dE}{dx}\right) \tag{14}$$

with randomly chosen value $\delta(dE/dx)$ from a gaussian distribution $G(\mu = 0, \sigma_{dE/dx})$.

4.7   Cherenkov Angle Parametrization

Basic theoretical information about the origin of Cherenkov radiation can be found elsewhere and will not be discuss here. The Cherenkov angle defined as the opening angle of the cone of radiation relativ to the direction of the incident charged particles momenta in medium with refractive index n is given by the expression

$$\theta_C = \arccos\left(\frac{1}{\beta \cdot n}\right) \tag{15}$$

with $\beta = p \cdot c/E$ being the velocity of the particle. Obviously computation of the expected Cherenkov angle for any given particle detected by the specific detector is straight forward. Key ingredient of the parametrization of the detector response is the resolution estimation. In case of DIRC detectors experience from the working device in the BaBar experiment tells us that the overall reconstruction resolution of the Cherenkov angle can be based on a single photon resolution $\sigma_{\mathrm{s.phot.}} \approx 10$ mrad. Responsible for the overall resolution then exclusively is the number of detected Cherenkov photons N through

$$\sigma_{\mathrm{tot}} = \frac{\sigma_{\mathrm{s.phot.}}}{\sqrt{N}},$$

which is simple count statistics. This number N has to be estimated and depends on

- the number of generated photons

$$N_0 = 2\pi \cdot \alpha \cdot L \left(\frac{1}{\lambda_{\min}} - \frac{1}{\lambda_{\max}}\right) \cdot \sin^2\theta_C = 2\pi \cdot \alpha \cdot L \left(\frac{1}{\lambda_{\min}} - \frac{1}{\lambda_{\max}}\right) \cdot \left(1 - \frac{m^2 + p^2}{p^2 \cdot n^2}\right) \tag{16}$$

with parameters

726   − fine structure constant α

727   − trajectory length L in the radiator material

728   − mass and momentum m and p of the incident track

729   − wave length region $\lambda_{\min}$ and $\lambda_{\max}$ where the photon detector is sensitive and

730   − refraction index n

731   • the trapping fraction r_{trap} which is the fraction of the photons kept in the radiator/lightguide
732   due to total reflection and

733   • the detection efficiency ϵ of the photon detector, e.g. a photo multiplier tube (PMT)

734 In order to derive the path length L in the material one has to distinguish between the different
735 Cherenkov devices.

736 In case of the **Barrel DIRC** on first of all has to compute the curvature due to the motion of a
737 charged particle in a magnetic solinoidal field $B = B_z$. The radius r of the circular shape in (x, y)
738 projection is given by

$$r = \frac{p_t}{q \cdot B} = \frac{3.3356 \cdot p_t \ [\text{GeV}/c]}{B \ [\text{T}]}. \tag{17}$$

739 for a particle with charge $q = \pm e$ and transverse momentum $p_t = p \cdot \sin\theta$. Based on this one can
740 calculate the entering angle ψ in ϕ direction to

$$\psi = \arccos\frac{r_B}{2 \cdot r} \tag{18}$$

741 with r_B being the radius of the DIRC Barrel i.e. the distance between the bars and the beam
742 line. Here it is obvious that particles with $2 \cdot r < r_B$ will not hit the detector at all defining a
743 minimum transverse momentum $p_{t,\min}$. The path length after some geometrical considerations
744 then computes to

$$L \approx d_{\mathrm{bar}} \cdot \sqrt{\frac{1}{\sin^2\theta} + \frac{1}{\tan^2\psi}} \tag{19}$$

745 where d_{bar} is the thinkness of the radiator bars and θ the dip angle of the helix of the track. The
746 expression is an approximation because curvature within the bar has been neglected. This leads
747 to significant wrong values for particles with $2 \cdot r \approx r_B$.

748 For the **Disc DIRC** and the **RICH** computing the radiator path length is much simpler. Here
749 L only depends on the dip angle and the radiator thinkness d_{rad} resulting in

$$L = \frac{d_{\mathrm{rad}}}{\cos\theta}. \tag{20}$$

750 Also here no curvature within the radiators has been taken into account. This anyway would lead
751 to more complicated estimates since angular changes along the radiator path results in systematic
752 worsening of the Cherenkov angle which is neglected completely.

753 Finally we still need the trapping fraction r_{trap} to determine the number of detected photons. There
754 is no known analytic expression to compute this, thus 2 dimensional lookup tables $r_{\mathrm{trap}}(\theta, p)$ for
755 every particle species have been prepared. Figure 44 shows as an example the trapping fraction
756 in the Barrel DIRC bars for muons and protons as a function of momentum p and dip angle θ.
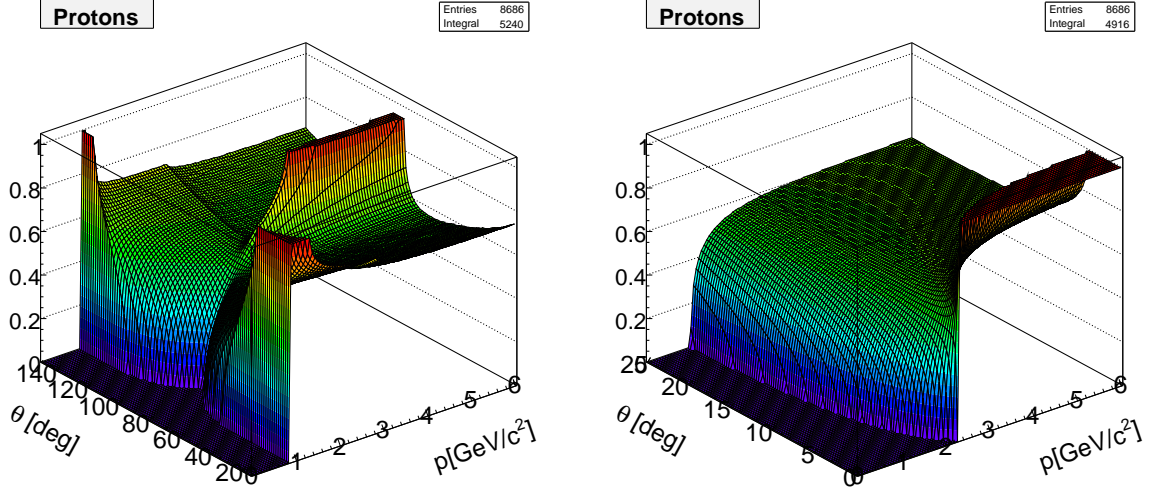
Figure 44: 2-dimensional picture of the trapping fraction for protons in the Barrel DIRC (left) and the Disc DIRC as a function of momentum p and dip angle θ.

With the path length L one can evaluate expression (16) so that the detected number of photons can be estimated to

$$N = N_0' \cdot \epsilon \cdot r_{\text{trap}} \tag{21}$$

where the N_0' is randomly generated from Poisson distibution with input value $\lambda = N_0$. This directly leads to the expected resolution σ_{tot} which is taken as the absolute uncertainty of the measurement of the Cherenkov angle. The simulated measured Cherenkov angle thus has been computed with formula (15) to

$$\theta_{C,\text{sim}} = \theta_C + \delta\theta_C \tag{22}$$

with randomly chosen value $\delta\theta_C$ from a gaussian distribution $G(\mu = 0, \sigma_{\text{tot}})$.

4.8   Time Of Flight Parametrization

From the geometrical point of view the calculation of the expected time of flight of a particle has similarities to the considerations done in 4.7 for the Barrel DIRC, since the TOF detector has also cylindrical shape. This requires also the particles with curvatures given by equation (17) to have a minimum transverse momentum p_t to reach the detector and produce a signal.

In order to compute the time of flight $t_{\text{TOF}} = s/v$ one in principal only needs the traveled distance s and the velocity v of the particle. While the latter one is simple to get by via the particles $\beta = p \cdot c/E$, the distance is not so easy to calculated due to the tracks curvature in the magnetic field. Nevertheless the calculation can be simplified exploiting the fact that the particles motion in z direction is independent of that one in th (x, y) plane. Therefore t can also be calculated via the ratio of the travelled angle Φ and the angular velocity ω

$$t_{\text{TOF}} = \frac{\Phi}{\omega} = \frac{1}{\omega} \cdot 2\arcsin\frac{r_B}{2r} \tag{23}$$
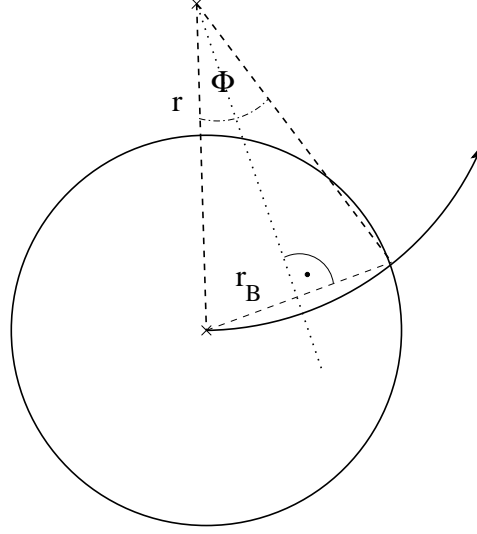
Figure 45: Projection of particle trajectory to (x, y) plane in order to determine Φ.

with the determination of Φ illustrated in fig. 45. The angular velocity in the projected plane is given by

$$\omega = \frac{B}{3.3356 \cdot E} \tag{24}$$

for a magnetic field B [T] and E [GeV]. With these expressions one can derive the true expected time of flight. What now has to be simulated is the expected accuracy of the measurement achieved by the detector. This depends on the time resolution assumed to be $\sigma_t \approx 100$ ps on one hand and on the resolution connected to track reconstruction on the other hand since the transverse momentum $p_t = p \cdot \sin(\theta)$ is needed to compute the flight length. Only a relative uncertainty $\sigma_p = \delta p / p \approx 2\%$ for the reconstructed absolute value of the momentum has been taken into account with respect to this, neglecting errors in polar angle measurement.

This results in measured values

$$t'_{\text{TOF}} = t_{\text{TOF}} + \delta t \tag{25}$$
$$p' = p \cdot (1 + \delta p) \tag{26}$$

with gaussian distributed deviations δt and δp according to $G(\mu = 0, \sigma_t)$ and $G(\mu = 0, \sigma_p)$. The primes denote from now the 'measured' or 'simulated' quantities. Now one basically has to reverse the process from above to get the simulated reconstructed value for the energy E needed to compute the squared mass

$$m'^2 = E'^2 - p'^2 \tag{27}$$

which acts as the observable of the TOF detector. Starting point is eq. (24) which forms to $E' = B/(3.3356 \cdot \omega')$ etc. The resulting term depending only on the quantities t'_{TOF}, p' and θ looks like

$$m'^2 = \left(\frac{B \cdot t'_{\text{TOF}}}{2 \cdot 3.3356 \cdot \arcsin\left(\frac{r_B}{2 \cdot 3.3356 \cdot p' \sin(\theta)} \right)} \right)^2 - p'^2 \tag{28}$$

4.9 Parameter Settings

Tab. 6 presents the complete set of relevant parameters which were used in the Fast Simulation to extract most of the results presented in this note, in particular in section 5.3.

Meaning	Quantifier	Value
Global		
Magnetic Field Strength	$B = B_z$	2 T
Relative Momentum Resolution	σ_p/p	1 %
Micro Vertex Detector (MVD)		
Angular Acceptance	$[\theta_{\min}; \theta_{\max}]$	$[0.0°; 180.0°]$
Relative dE/dx Resolution	$\sigma_{dE/dx}$	22 %
Straw Tube Tracker (STT)		
Angular Acceptance	$[\theta_{\min}; \theta_{\max}]$	$[7.765°; 159.44°]$
Relative dE/dx Resolution	$\sigma_{dE/dx}$	20 %
Inner Radius	R_I	15 cm
Time Projection Chamber (TPC)		
Angular Acceptance	$[\theta_{\min}; \theta_{\max}]$	$[7.765°; 159.44°]$
Relative dE/dx Resolution	$\sigma_{dE/dx}$	8 %
Inner Radius	R_I	15 cm
Barrel DIRC		
Angular Acceptance	$[\theta_{\min}; \theta_{\max}]$	$[22.0°; 140.0°]$
Inner Radius	R_I	48 cm
Single Photon Resolution	σ_{ph}	10 mrad
Thickness of Slab	d_S	1.7 cm
Refractive Index of Quarz	n_Q	1.472
Total Photon Detector Efficiency	ϵ_{PD}	7.5 %
Disc DIRC		
Angular Acceptance	$[\theta_{\min}; \theta_{\max}]$	$[5.0°; 22.0°]$
Single Photon Resolution	σ_{ph}	10 mrad
Thickness of Disc	d_D	1.7 cm
Refractive Index of Quarz	n_Q	1.472
Total Photon Detector Efficiency	ϵ_{PD}	7.5 %
Ring Image Cherenkov Detector (RICH)		
Angular Acceptance	$\theta_{\min}$	0.0°
	$\alpha_{\max}$ (vert.)	5.0°
	$\alpha_{\max}$ (hor.)	10.0°
Single Photon Resolution	σ_{ph}	10 mrad
Thickness of Radiator	d_D	1 m
Refractive Index of Radiator	n_R	1.05
Total Photon Detector Efficiency	ϵ_{PD}	7.5 %
Time of Flight system (TOF)		
Angular Acceptance	$[\theta_{\min}; \theta_{\max}]$	$[22.0°; 140.0°]$
Inner Radius	R_I	38 cm
Total Time Resolution	σ_t	141 ps

Table 6: Parameter Settings used for the Fast Simulation

5   Evaluation

5.1   Potential of the Subsystems

5.2   Matching of the Subsystems

5.3   Maps of Separation

In order to evaluate the PID performance applied to specific physics channels the information about

1. kinematic distribution of signal channel

2. kinematic distribution of possible bakcground

3. separation power in phase space

have been combined in the way, that signals distributions for every particle species have been projected on the according map of separation power with either STT or TPC option. Since the implementation of the TOF detector is still under investigation at the time of writing, the studies for both options also have been performed without the information of the TOF system.

Background has been taken into account by punching the according separation map with its distribution leaving only regions colored where in fact background particles appear.

For instance to determine the PID quality for kaons from $\bar{p}p \to D^+ D^- \gamma$ reactions at a particular energy against pions from DPM background, the phase space histogram of kaons from the signal channel has been projected on the $\pi^\pm - K^\pm$ separation map which has been punched with the distribution of pions from DPM events at the same total energy.

This procedure gives access to the information how good a particle type for a specific signal channel can be identified. In particular it offers the possibility to identify regions with insufficient PID quality. As a quantitative measure for the goodness or badness of a certain projection two quantities have been determined:

1. the fraction of the signal f where separation power is $N_\sigma < 8$

2. the average σ_{avg} for that region

As an arbitrary criterion all projections fulfilling

$$f > 0.2 \quad \&\& \quad \sigma_{\mathrm{avg}} < 5\sigma \qquad \text{or} \qquad f > 0.5$$

have been listed as problematic cases. Tab. 7 contains all channels with $\bar{p}$ momentum below 8.7 GeV/c, tab. 8 shows channels with $p_{\bar{p}} > 8.7$ GeV/c. In order to assign additional structure to this vast amount of information the numbers have been colored according to the severeness of PID deficiency. Since intuitively higher values f and smaller values σ_{avg} can be considered as bad

and vice versa smaller fractions f and larger σ_{avg} are considered as good, the coloring scheme was chosen as:

$$f \quad = \quad 0\ldots30 \quad \boxed{\ldots40} \quad \boxed{\ldots50} \quad \boxed{\ldots60} \quad \boxed{\ldots70} \quad \boxed{\ldots80} \quad \boxed{\ldots90} \quad \boxed{\ldots100}\,\%$$

$$\sigma_{\mathrm{avg}} \quad = \quad \boxed{0\ldots1.5} \quad \boxed{\ldots2.0} \quad \boxed{\ldots2.5} \quad \boxed{\ldots3.0} \quad \boxed{\ldots3.5} \quad \boxed{\ldots4.0} \quad \boxed{\ldots4.5} \quad \ldots5.0\,\sigma$$

with values marked red being worse than values marked green or yellow. The four different combinations (f,σ) correspond to the combinations

1. TPC option including TOF

2. STT option including TOF

3. TPC option w/o TOF

4. STT option w/o TOF

i. e. to contrast TPC and STT PID performance compare either (f_1,σ_1) and (f_2,σ_2) with TOF or (f_3,σ_3) and (f_4,σ_4) without TOF. The PID hypothesis column has always been colored with the 'worst' color in the row in order to easier spot separation problems between particular hypothesis.

Figs. 46 – 48 present the corresponding plots for some selected channels. Each column shows the results for one particular channel and the four different detector setups in the same order from top to bottom as given in the list. In tabs. 7 and 8 those channels are marked with a bullet (•) in the PID column.
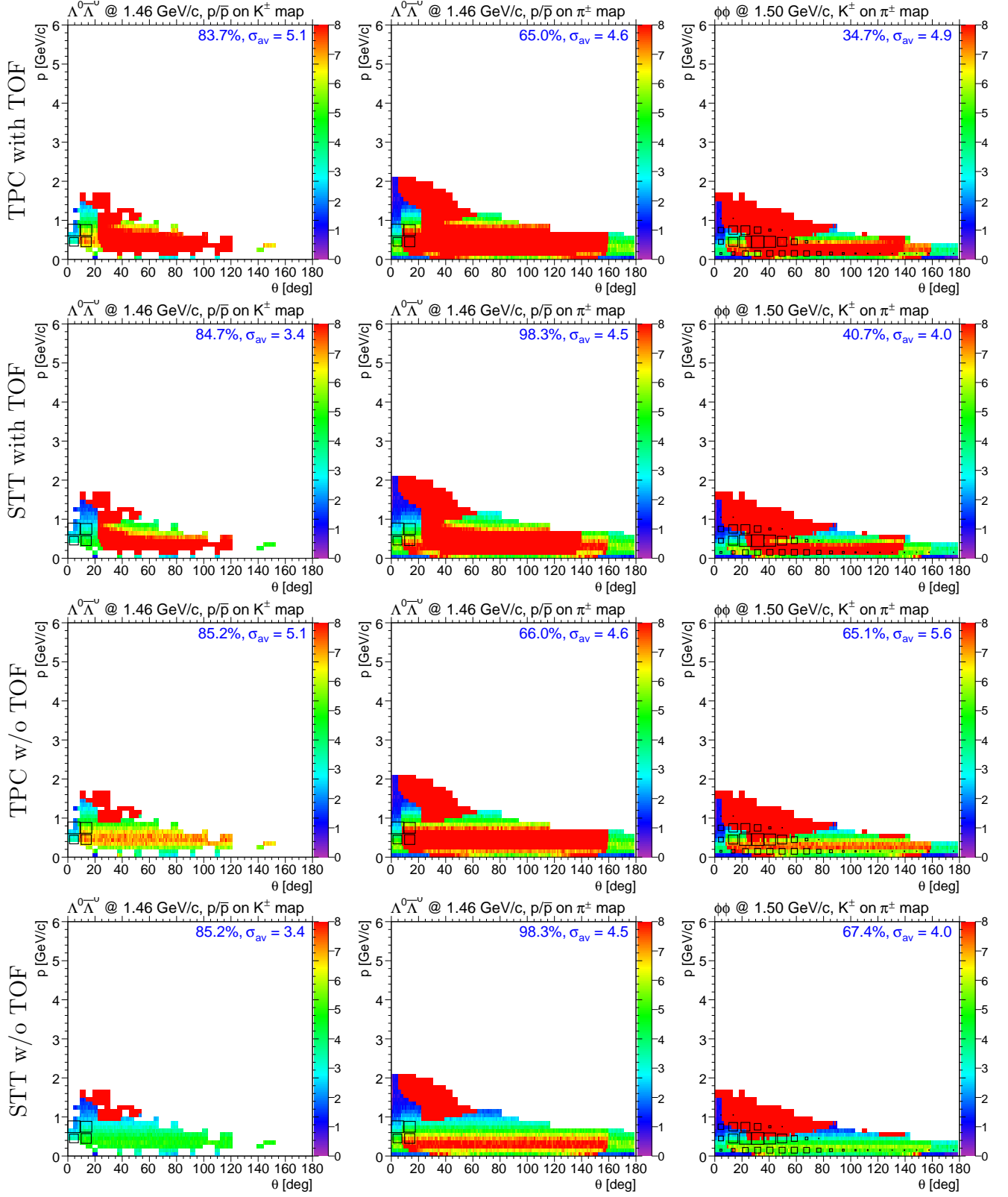
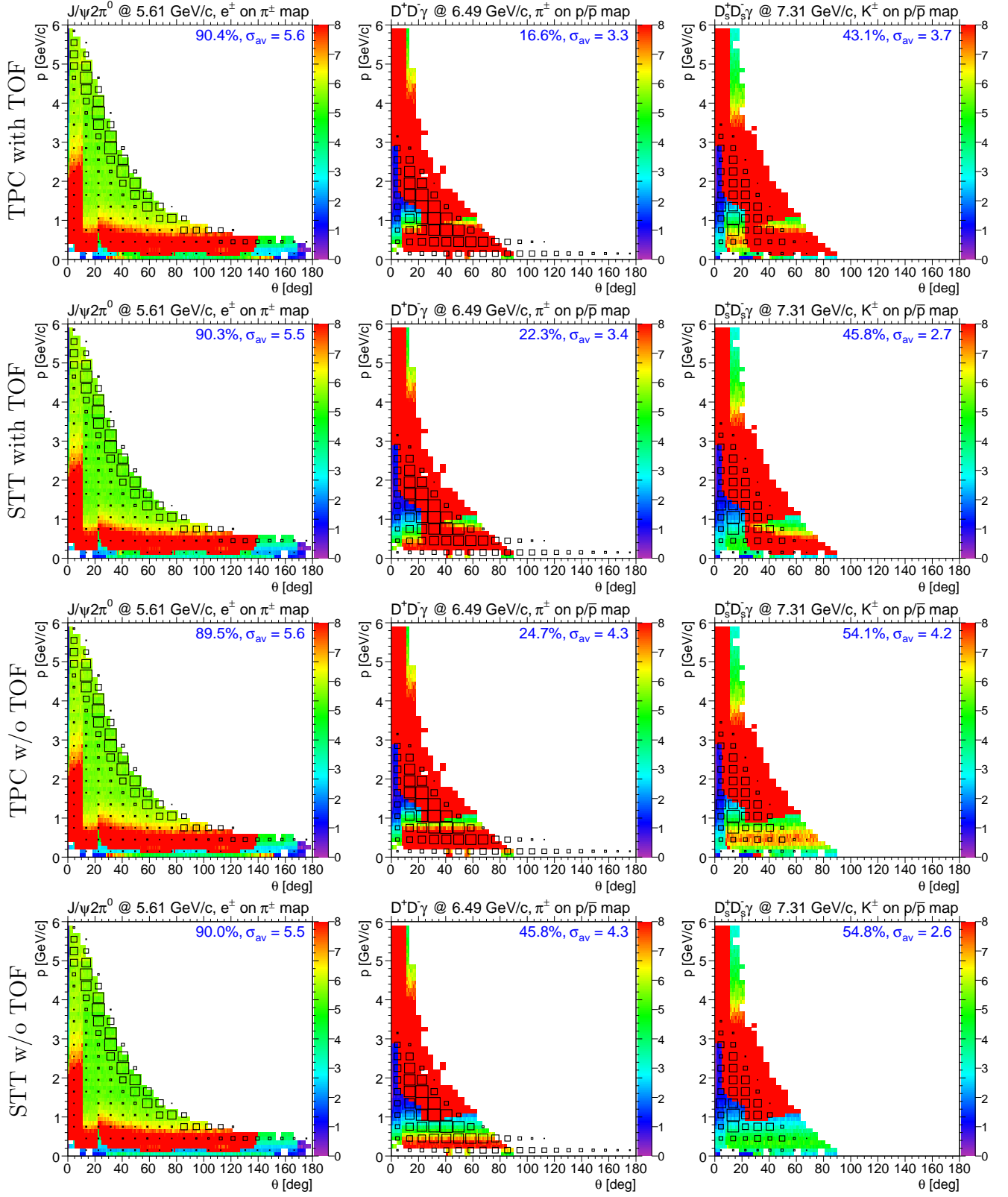Figure 46: Projection of kinematic distributions on separation maps (1).

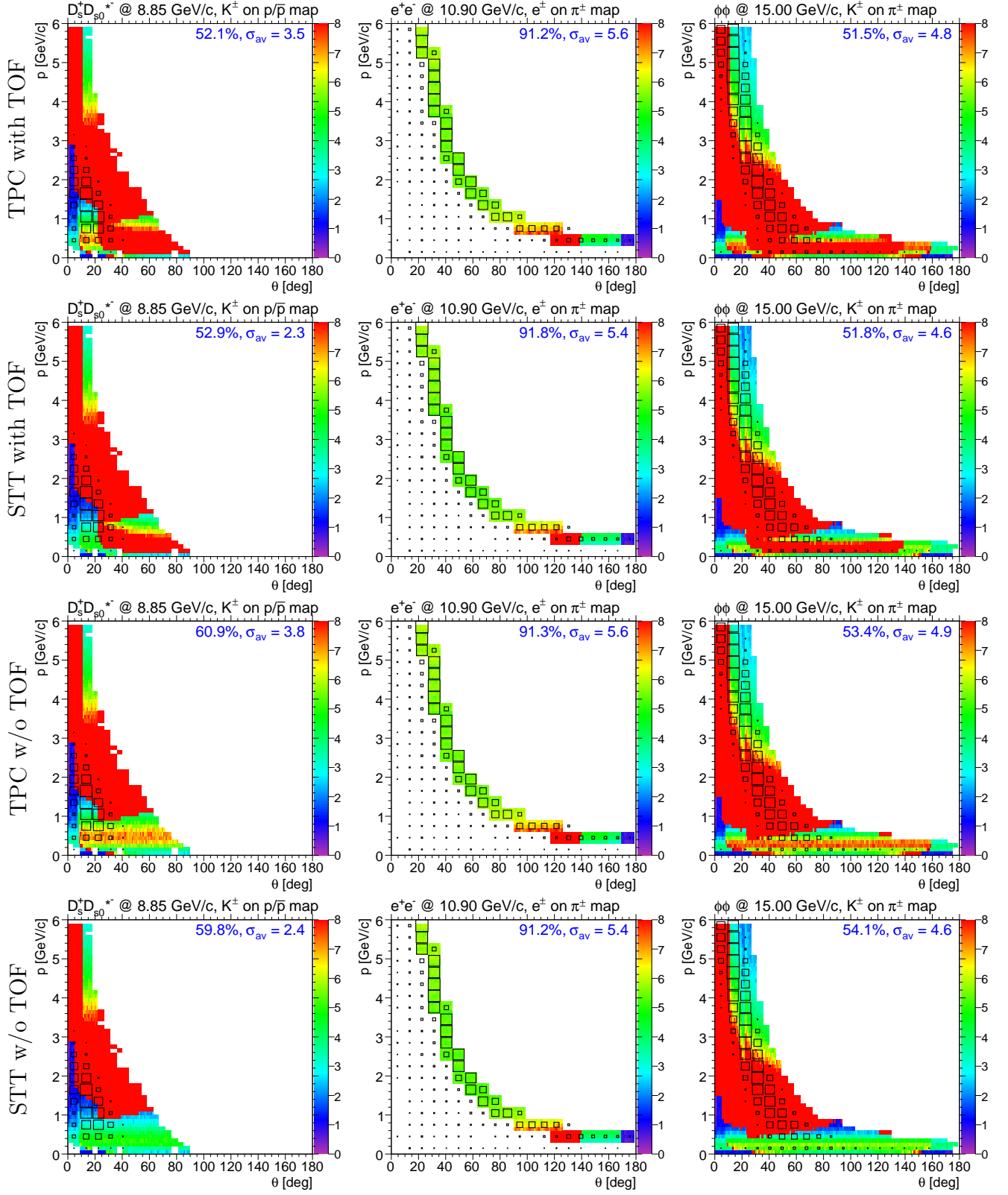Figure 47: Projection of kinematic distributions on separation maps (2).

Figure 48: Projection of kinematic distributions on separation maps (3).

$p_{\bar{p}}$ [GeV/c]	Signal	PID	f_1 [%]	σ_1	f_2 [%]	σ_2	f_3 [%]	σ_3	f_4 [%]	σ_4
1.460	$\Lambda^0\bar{\Lambda}^0$	π - e	64	4.0	64	3.3	64	3.7	66	2.9
		π - μ	30	2.6	30	2.5	31	2.5	30	2.3
		p - e	49	5.3	72	5.6	50	5.3	72	5.6
		p - π ●	63	4.6	98	4.5	65	4.6	98	4.5
		p - K ●	85	5.1	85	3.4	84	5.0	84	3.4
1.500	$\phi\phi$	K - π ●	34	4.9	41	4.0	65	5.6	65	4.0
1.700	e^+e^-	e - π	91	5.9	92	5.6	91	5.9	92	5.6
3.300	e^+e^-	e - π	93	5.7	93	5.5	94	5.7	93	5.5
5.609	$J/\psi 2\pi^0$	e - π ●	90	5.7	89	5.5	90	5.6	90	5.5
		μ - π	92	1.3	92	1.2	92	1.2	92	1.2
	$J/\psi\pi^+\pi^-$	e - π	88	5.7	88	5.5	88	5.6	89	5.5
		μ - π	92	1.3	91	1.2	92	1.3	92	1.2
6.080	$J/\psi\eta$	e - π	65	5.6	64	5.5	65	5.6	65	5.5
6.232	$J/\psi 2\pi^0$	e - π	90	5.6	89	5.5	89	5.6	89	5.5
		μ - π	93	1.3	92	1.2	92	1.2	92	1.2
	$J/\psi\pi^+\pi^-$	e - π	90	5.6	91	5.5	91	5.6	91	5.5
		μ - π	93	1.3	94	1.2	94	1.2	94	1.2
6.488	$D^+D^-\gamma$	π - p ●	16	3.4	21	3.5	25	4.5	45	4.3
		K - p	23	4.0	27	3.4	38	4.9	38	3.0
6.988	$J/\psi\pi^+\pi^-$	e - π	92	5.6	93	5.5	93	5.6	93	5.5
		μ - π	96	1.2	96	1.2	96	1.2	96	1.2
6.990	$J/\psi\eta$	e - π	77	5.6	77	5.5	77	5.6	77	5.5
7.314	$D_s^+D_s^-\gamma$	π - p	13	4.1	23	4.6	21	4.9	43	4.8
		K - p ●	42	3.7	44	2.7	54	4.2	54	2.6
7.746	$D^{*+}D^{*-}\gamma$	π - K	17	4.2	18	3.9	20	4.5	21	3.7
		π - p	24	4.8	27	4.8	28	4.9	38	4.8
		K - p	14	5.0	17	4.7	24	5.4	25	3.4
	$D_s^+D_s^-\gamma$	π - p	13	4.0	23	4.4	19	4.8	40	4.8
		K - p	41	3.6	43	2.7	51	4.1	51	2.6
7.900	e^+e^-	e - π	91	5.6	91	5.5	91	5.6	91	5.5
8.000	$\Lambda^0\bar{\Lambda}^0$	π - K	22	4.2	24	3.2	35	5.2	36	3.5
		π - p	35	3.8	49	3.8	45	4.4	80	4.6
	$D^{*0}\bar{D}^{*0}\gamma$	K - p	10	6.5	13	5.9	19	6.1	20	4.2
	$D^+D^-\gamma$	π - p	17	3.4	22	3.5	25	4.4	44	4.3
		K - p	23	4.0	26	3.3	36	4.6	35	3.0
	$D^0\bar{D}^0\gamma$	K - p	13	6.1	17	5.6	23	5.9	22	4.4
	$D_s^+D_s^-\gamma$	π - K	12	4.9	14	3.7	20	5.4	20	3.6
		π - p	13	4.1	23	4.5	22	4.8	41	4.8
		K - p	40	3.6	43	2.6	50	4.0	51	2.6
	$D^{*+}D^{*-}\gamma$	π - K	22	4.0	23	3.5	25	4.4	26	3.3
		π - p	26	4.3	31	4.6	29	4.5	40	4.6
		K - p	13	5.1	17	4.5	25	5.4	24	3.6
8.682	$J/\psi\pi^+\pi^-$	e - π	91	5.6	93	5.5	92	5.6	93	5.5
		μ - π	96	1.3	96	1.2	96	1.3	96	1.2
	$J/\psi 2\pi^0$	e - π	92	5.6	92	5.5	92	5.6	92	5.5
		μ - π	96	1.3	96	1.2	96	1.3	96	1.2

Table 7: Table of projection results (1). Marked channels (●) appear in figs. 46 – 48.

$p_{\bar{p}}$ [GeV/c]	Signal	PID	f_1 [%]	σ_1	f_2 [%]	σ_2	f_3 [%]	σ_3	f_4 [%]	σ_4
8.700	$J/\psi\eta$	e - π	90	5.6	91	5.5	90	5.6	90	5.5
8.847	$D_s^+ D_{s0}^{*-}$	π - p	5	4.4	9	5.0	11	5.2	20	4.5
		K - p ●	53	3.4	53	2.3	59	3.8	61	2.4
10.000	$\Lambda^0 \bar{\Lambda}^0$	π - K	17	4.0	20	3.1	28	5.0	28	3.4
		π - p	32	3.5	43	3.4	41	4.3	71	4.3
		p - π	17	5.6	19	5.4	19	5.5	23	5.0
10.295	$J/\psi 2\pi^0$	e - π	93	5.6	93	5.5	92	5.6	93	5.5
		μ - π	97	1.3	97	1.2	97	1.3	97	1.2
	$J/\psi \pi^+\pi^-$	e - π	93	5.6	93	5.5	93	5.6	93	5.5
		μ - π	98	1.3	98	1.2	98	1.3	98	1.2
10.900	e^+e^-	e - π ●	90	5.6	91	5.5	91	5.6	91	5.4
12.000	$D^{*0}\bar{D}^{*0}\gamma$	π - p	10	5.8	12	5.6	13	5.9	20	5.0
		K - p	20	5.4	22	5.2	27	5.5	28	4.4
	$D_s^+ D_s^- \gamma$	π - p	16	4.1	23	4.0	22	4.6	38	4.5
		K - p	33	3.4	34	2.7	39	3.8	40	2.6
	$\phi\phi$	K - π	41	5.3	41	5.1	44	5.3	44	5.0
	$D^+ D^- \gamma$	π - p	17	3.6	22	3.5	24	4.3	38	4.2
		K - p	26	4.1	27	3.5	33	4.5	34	3.3
	$D^0 \bar{D}^0 \gamma$	π - p	11	5.6	14	5.5	15	5.6	22	4.8
		K - p	22	5.1	24	5.0	29	5.3	29	4.3
	$D^{*+} D^{*-} \gamma$	π - K	31	4.4	32	3.4	34	4.5	33	3.4
		π - p	24	4.4	37	5.1	27	4.8	45	5.1
		K - p	22	4.9	24	4.6	30	5.2	30	4.0
	$\phi\phi$	K - π	41	5.3	42	5.1	44	5.3	44	5.0
12.349	$J/\psi 2\pi^0$	e - π	93	5.6	93	5.5	93	5.6	93	5.5
		μ - π	98	1.3	98	1.2	98	1.3	98	1.2
	$J/\psi \pi^+\pi^-$	e - π	93	5.6	93	5.5	93	5.6	93	5.5
		μ - π	98	1.3	98	1.2	98	1.3	98	1.2
15.000	$D^+ D^- \gamma$	π - μ	22	3.3	22	3.2	22	3.2	23	3.3
		π - p	17	3.5	20	3.4	22	4.3	35	4.1
		K - p	24	4.1	26	3.5	30	4.3	31	3.2
	e^+e^-	e - π	90	5.6	89	5.4	89	5.6	90	5.5
	$D^{*+} D^{*-} \gamma$	π - μ	30	3.6	30	3.6	31	3.6	30	3.7
		π - K	25	3.9	26	3.0	27	4.1	28	2.9
		π - p	21	4.1	36	4.8	25	4.4	43	4.8
		K - π	22	5.3	22	5.1	24	5.4	24	5.0
		K - p	21	4.6	23	4.3	27	4.9	27	3.9
	$D^{*0}\bar{D}^{*0}\gamma$	K - p	19	5.1	20	4.8	25	5.3	25	4.2
	$\phi\phi$	K - π ●	51	4.8	52	4.7	54	4.9	53	4.6
	$D_s^+ D_s^- \gamma$	π - μ	23	3.4	22	3.3	22	3.4	23	3.4
		π - p	17	3.9	22	3.8	22	4.4	36	4.3
		K - p	30	3.3	30	2.8	34	3.7	34	2.7
	$\phi\phi$	K - π	51	4.8	52	4.6	53	4.9	53	4.5
	$D^0 \bar{D}^0 \gamma$	K - π	24	5.4	24	5.1	25	5.4	26	5.0
		K - p	18	5.0	20	4.6	24	5.2	24	4.1

Table 8: Table of projection results (2). Marked channels (●) appear in figs. 46 – 48.

6   Global PID Scheme

The PANDA spectrometer will feature a complete set of innovative detectors for particle identification. The detection of neutral particles will be performed by a highly granular electromagnetic calorimeter. Charged particles will be identified in the low momentum region by their energy deposit and ToF, in all other momentum regions by innovative DIRC detectors. The target spectrometer will be complemented by a forward spectrometer to detect high momentum particles and surrounding muon detectors. Each detector systems performance is optimised in itself. Studies have begun to combine the responses of various detectors in a common framework based on a likelihood scheme or a carefully trained neutral network. These combined likelihood schemes are successfully employed at various detector systems like HERMEs, Belle and BaBar. They rely on a reliable parametrisation of the detector component response from simulation and test-beams. This has to be taken into account in testing PANDA's individual components. The combined performance of the system will be significantly better than the individual separation powers.

7   Conclusion

In this report of the PANDA PID TAG

all informations about the PID detectors of PANDA and their performance are gathered.

the separation power is declared as the indication to determine the detector performance

the Fast Simulation was explained as the tool for the overall treatment.

parameterizations to evaluate Separation Power Maps we described. Simulations for some of the subsystems with other tools than the Fast Simulation verify the correctness of the approach with the Fast Simulation.

Parameters (f and σ_{avg}) were found to evaluate the ability of detectors and systems.

The Pid TAG gives no recommendations but numbers and a clue how to read them. They are strong and serve as a basis for decisions to be take by the PANDA collaboration.

8   Acknowledgments

References

[1] P̄ANDA Collaboration, Technical Progress Report, FAI R-ESAC/Pbar 2005

[2] http://panda-wiki.gsi.de/cgi-bin/viewauth/Tagpid/WebHome, Wiki page of the P̄ANDA PID TAG

[3] F. Sauli, Nucl. Instrum. Meth. **A386**, 531 (1997)

[4] R. Aleksan et al., Nucl. Inst. Meth. **A397**, 261 (1997)

[5] A. Galoyan, V.V. Uzhinsky, AIP Conf. Proc. 796, pp. 79-8 2, 2005

[6] P. Schönmeier et al., to appear in the proceedings of 6th In ternational Workshop on Ring Imaging Cherenkov Counters (RICH 2007), Trieste, It aly, 15-20 Oct 2007.

[7] W.-M. Yao et al. 2006 J. Phys. G: Nucl. Part. Phys. **33** 1

9 Appendix

Members of the PID TAG

- G. Schepers, C. Schwarz - Barrel Dirc (Chairs)

- B. Kopf, R. Novotny - Barrel Calorimeter

- B. Seitz - Cherenkov Counter (Global PID)

- O. Denisov / M. P. Bussa - Muon Counter

- K. Föhl / P. Vlasov - Forward Cherenkov

- J. Smyrski / O. Wronska - Forward Calorimeter

- Q. Weitzel / S. Neubert - Time Projection Chamber

- C. Schwarz, A. Galoyan - Time of Flight

- K. Götzen - Fast Simulation

- K. Peters - Physics